Influence of sintering on particulate fouling of heat exchangers

Clevers, S.H.

Award date:
2004

INFLUENCE OF SINTERING ON PARTICULATE FOULING OF HEAT EXCHANGERS

S.H. Clevers

August, 2004
Report Nr. WET 2004

Supervisors:
M.Sc. M.S. Abd-Elhady
dr.ir. C.C.M. Rindt
prof.dr. A.A. van Steenhoven

Eindhoven University of Technology
Department of Mechanical Engineering
Division Thermo Fluids Engineering
Section Energy Technology

Samenvatting

Vervuiling van warmtewisselaars kan leiden tot ernstige technische en economische problemen in the industrie. Twee type vervuilingslagen aan de gas zijde van de warmtewisselaar kunnen worden gekarakteriseerd, namelijk poedervormige en gesinterde vervuilingslagen. De vervuilingslaag blijft poedervormige als de temperatuur beneden de minimum sintering temperatuur blijft. De vervuilingslaag zal verandering in een stevige poreuze structuur als de temperatuur aan de gas zijde van de warmtewisselaar de minimum sintering temperatuur overschrijdt. De invloed van sintering op de vervuiling van warmtewisselaars in experimenteel onderzocht. Sintering start nekvorming op de contact punten tussen deeltjes. Door de nekvorming kunnen de deeltjes in de gesinterde vervuilinslaag alleen als een geheel bewegen, hierdoor worden de energieverliezen door botsende deeltjes verlaagd en blijven minder deeltjes plakken. Verder reduceert nekvorming de verwijdering van deeltjes uit gesinterde oppervlakkken, omdat er meer energie nodig is om de verbindingen tussen de deeltjes te verbreken. Sintering beinvloedt de groeisnelheid van de vervuilingslaag door de mate van depositie en verwijdering van deeltjes te verlagen. Sintering verlaagt de porositeit en verbetert de contact punten tussen de deeltjes. Beide zijn voordelig voor de warmteoverdracht door de vervuilingslaag. Sintering verandert de microstructuur van een vervuilingslaag in een sterke compacte structuur. Dit kan verkomen worden als de temperatuur van de gas zijde van de warmtewisselaar beneden de minimum sintering temperatuur blijft. De kracht nodig om de verbindingen tussen de deeltjes uit een gesinterde laag te verbreken is afhankelijk van de mate van sintering. Deze kracht kan gemodelleerd worden door gebruik te maken van sintering modellen die nekgroei beschrijven. De kracht kan geimplementeerd worden in modellen die verwijdering van deeltjes beschrijven door botsingen.

Abstract

Fouling of heat exchanger surfaces causes serious technical and economical problems in the industry. Two types of fouling layers on the gas-side of the heat exchanger can be distinguished, namely powdery and sintered fouling layers. The fouling layer remains powdery if the gas-side temperature is below the minimum sintering temperature. The fouling layer will change into a robust porous structure, if the gas-side temperature exceeds the minimum sintering temperature. The influence of sintering on fouling of heat exchangers is investigated experimentally. Sintering causes neck formation to start at the contact points between particles. Due to the neck formation, the particles in the sintered layer can only move as a whole, which consequently reduces the energy losses, due to an incident particle impact and therefore lower the sticking velocity. Furthermore, particle bonding reduces the particle removal by particle impaction, because more kinetic energy is necessary to break the bonding between particles. Sintering influences the growth rate of the fouling layer by lowering the particle deposition rate and removal rate. Sintering lowers the porosity and improves the contact between the particles, which are both beneficial for the thermal conductivity. Sintering change the microstructure of a fouling layer into a strong condense structure, this can be prevented if the gas-side temperature does not exceed the minimum sintering temperature of the fouling layer material. The breaking force necessary from breaking the bonding between particles depends on the degree of sintering. This force can be modelled using sintering models that predicts neck growth. The breaking force can be implemented in models that describe particle removal from sintered surfaces, due to an incident particle impact.

Contents

Chapter 1

Introduction

Heat recovery systems are used in a wide range of industrial processes to recover energy. Depending on the conditions in the heat recovery system, deposits can cover the heat exchanger surfaces. This process is known as particulate fouling. Particulate fouling is defined as the deposition of particles on a heat transfer surface to form an insulating layer, see figure 1.1

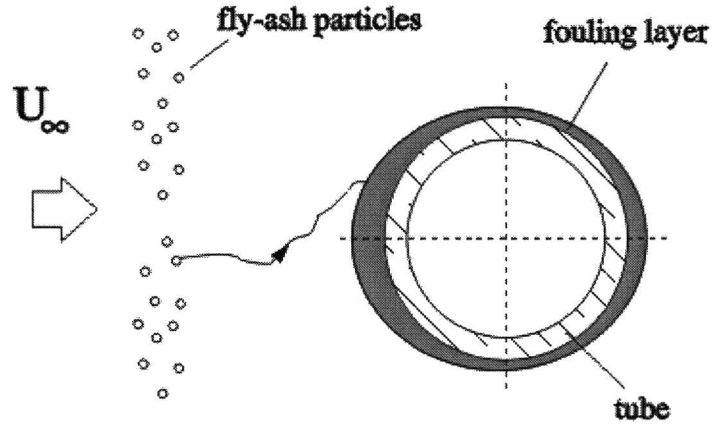

Figure 1.1: Particulation process for tube bundles placed in cross-flow with the flue gas stream [1].

Fouling of heat transfer surfaces causes serious technical and economical problems in the industry. The fouling layer decreases the rate of energy, which is recovered and can lead to failure of the operating system. Van Beek [1] found a decrease of 27% of the total recovered energy in a Dutch waste incinerator [1]. Van Beek [1] observed that the structure of the fouling layer depends on the position in the heat recovery system, see figure 1.2. The structure of the fouling layer of the economizer, where the gas temperature is the lowest, is thin and powdery, while on the super heater, where the gas temperature is the highest, a robust compact fouling layer is found.

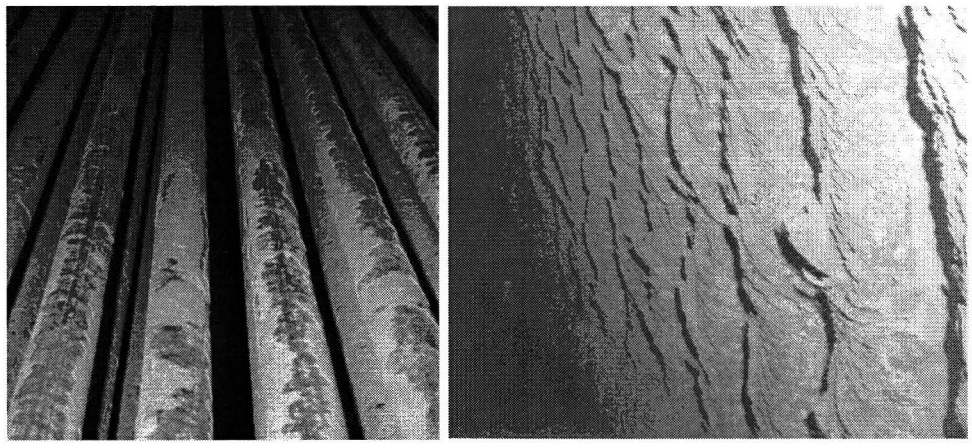

(a) (b)

Figure 1.2: Deposits observed on the tube [1]. (a) Economizer. (b) Superheater.

The high temperature causes neck formation to start in the fouling layer of the superheater. This phenomenon is known as sintering. Sintering is a complex mass transport mechanism, which can change a powder into a solid structure [2], see figure 1.3.
The working definition of sintering follows: *Sintering is a thermal treatment for bonding particles into a coherent, predominantly solid structure via mass transport events that often occurs on the atomic scale. The bonding leads to improved strength and lower system energy* [2]. Sintering starts when the temperature is above the minimum sintering temperature. The minimum sintering temperature is a boundary at which sintering is initiated.

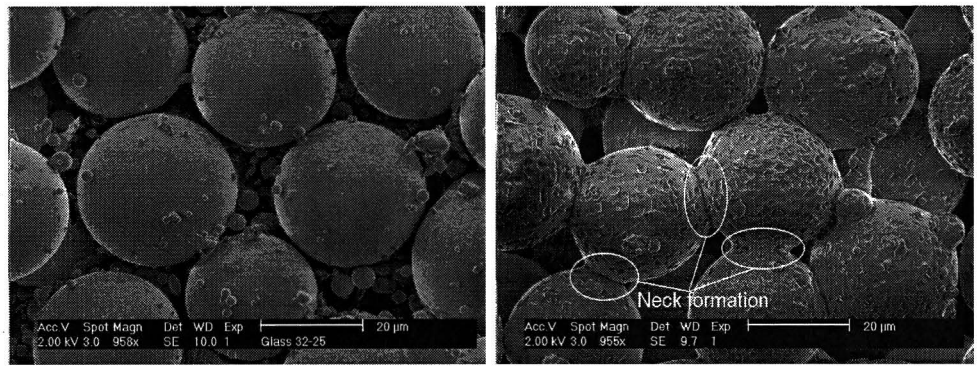

(a) (b)

Figure 1.3: (a) Powdery surface of glass particles. (b) Sintered surface of glass particles.

1.1 Problem definition and approach

To study the effect of sintering on the fouling mechanism in a heat recovery systems a research is set up. The goal of the research is to determine the influence of sintering on fouling of heat exchangers. Experiments are conducted to study this influence.
Particulate fouling causes fly ash particles to impact on heat exchanger tubes. Depending on the impact velocity, the incident particles may stick, rebound or remove other particles. To measure the influence of sintering on particle deposition and removal on and from a fouling layer, impaction experiments are conducted on different sintered surfaces.
In heat recovery system a temperature gradient is established between the top and bottom of a fouling layer, due to the hot flue gasses and the relatively cold heat exchanger tube. An experiment is set up to study the influence on the fouling layer structure when the temperatures in the temperature gradient exceed the minimum sintering temperature.
The minimum sintering temperature of a fouling layer from a biomass gasifier is measured and compared to the operating gas-side temperature of the gas cooler in the gasifier. Finally, the breaking force is introduced, which is necessary for breaking the bonds between the sintered particles. The breakage force is determined by modelling the neck growth.

1.2 Outline of this thesis

In the next chapter, essential background information of the sintering theory is given. Mass transport mechanisms, sintering models and sintering measurement techniques are discussed. Chapter 3 contains a description of the experimental methods, including impaction, temperature gradient, porosity and the minimum sintering temperature experiments. The results of the experiments are discussed in chapter 4. In chapter 5 the breaking force is presented. This thesis is ended in chapter 6 with conclusions and recommendations.

Chapter 2

Sintering theory

Sintering has been known for many centuries. Sintering was used by the Egyptian to make pottery and metal tools (3000 B.C.), the Chinese for making porcelain and the Inca for gold-platinum jewellery. Nowadays a wide range of products are made using the sintering process including dental implants, rocket nozzles, ultrasonic transducers and even golf clubs [2]. Although known for thousands of years, the first sintering models were developed in the 1930s and 1940s. The first models became the basis of our present understanding of the sintering mechanism [4]. The sintering process is understood qualitatively but the analytical models are inadequate to quantitatively predict the sintering behavior. Numerical models have been developed for accurate prediction of the sintering mechanism.
Sintering is a complex process because:

- Dimensions and material properties of the powder compact will change during the sintering process (porosity, density, strength, grain size, electrical resistivity, thermal conductivity) [5].
- Sintering is time and temperature dependant. A minimum temperature is needed to exceed the activation energy, which holds the atoms together. This minimum temperature is called minimum sintering temperature T_s
- Different mechanisms lead to different forms of sintering, solid state sintering, liquid sintering and viscous sintering and pressure assist sintering [6, 5].
- The sintering process can be forced by; curvature of the grain surface, externally applied pressure and a chemical reaction [6].

The mass transport mechanisms, which occur during the sintering process are explained in section 1.1. In section 1.2 sintering is described in three stages to simplify the sintering process. These three stages can be described with analytical models, see section 1.3. More advanced sintering models are discussed in section 1.4. The minimum sintering temperature is discussed in section 1.5. The measurement techniques to determine of degree of sintering are described in section 1.6.

2.1 Transport mechanisms

The solid-state sintering process can be distinguished in several transport mechanisms. Figure 2.1 shows the different solid-state mass transport mechanisms. There are two main categories, surface transport and volume transport [2]. Surface transport has lower activation energy compared to volume transport, therefore surface transport starts at lower temperatures. Surface transport is the movement of atoms or molecules on the surface of a particle, no densification occurs. Sintering without densification is called coarsening [2].
Amorphous materials, such as polymers and glasses, will sinter by viscous flow. If a liquid

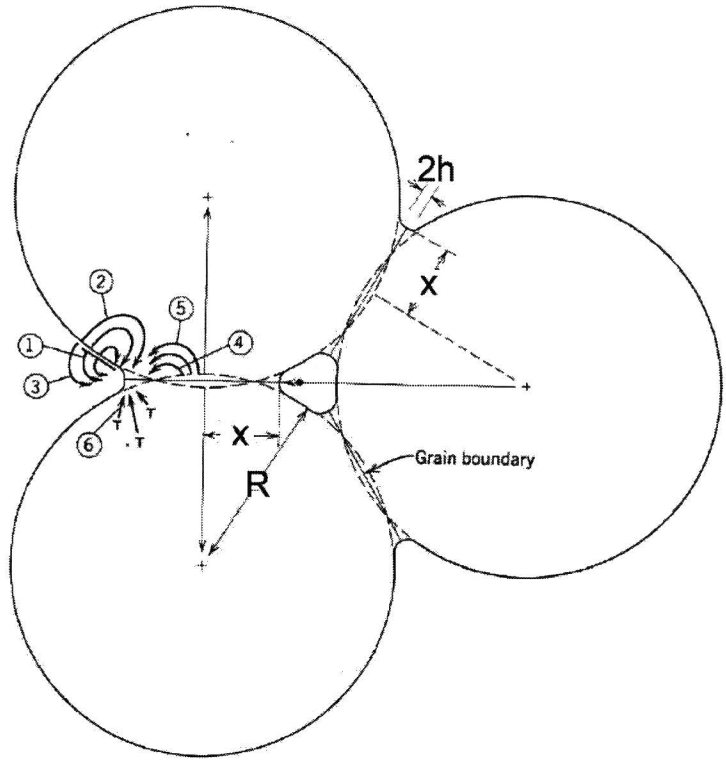

Figure 2.1: Mass transport mechanisms for polycrystalline materials. Where R is the grain radius, x is the neck radius, h is half the neck width. 1 surface diffusion, 2 volume diffusion surface, 3 vapor transport, 4 grain boundary diffusion, 5 volume diffusion, 6 plastic flow.

is present during the sintering process, liquid sintering takes place. The different mass transports will now be described in more detail.

2.1.1 Surface transport

Vapor transport

Vapor transport is a surface transport mechanism of atoms and molecules. The atoms or molecules evaporate at the surface of the grains and travel through the pore space to con-

tact points between particles [6]. Vapor transport repositions the atoms in order to reduce the surface energy [6]. Evaporation occurs preferentially at a convex curved surface (i.e. grain surface). The attraction between atoms at a convex curved surface is weaker than on a flat or concave curved surface. The atoms on a convex curved surface can therefore evaporate more readily [7]. Therefore the vapor pressure at the grain surface is higher than the vapor pressure at the neck. This is expressed by the Kelvin equation, see equation 2.1.

$$p - p_o = \frac{M\gamma_{sv}}{\rho R_c T}\left(\frac{1}{R}\right)p_o \tag{2.1}$$

With p_{vap} the vapor pressure on the curved surface, p_o the vapor pressure on a flat surface, γ the surface tension, M the molecular weight, T the absolute temperature, ρ the density, R_c the universal gas constant, and R the radius of curved surface.

Convex surfaces overpressure $(R > 0, (p - p_o) > 0)$
Concave surfaces underpressure $(R < 0, (p - p_o) < 0)$

The difference in vapor pressure is the driving force of vapor transport.

Surface diffusion

Surface diffusion is like vapor transport, a transport mechanism without densification. During surface diffusion a migration of atoms occurs from low curvature surfaces (grain surfaces) to high curvature surfaces (neck regions) [2].
At the atomic level the grain surface seems not to be smooth, it consists of defects. These defects are important for surface diffusion. If the temperature is high enough, atoms can break away from the existing bonds and travel in random direction on the grain surface. At the contact point between two particles a huge deflection of the grain surface is present. The deflection on the surface results in a higher defects density than on other parts. The difference in defect density is the driving force for surface diffusion. Therefore a migration of atoms occurs from the low curvature regions (grain surface) to the high curvature regions (i.e. neck) [2].

2.1.2 Volume transport

Volume diffusion

Volume diffusion is the migration of atoms through the grain volume to the neck as illustrated in Figure 2.1. Three different diffusion paths can be distinguished.

- (2) From the grain surface through the grain volume to the neck, no densification. This type of mass transport is known as volume diffusion surface. Theoretically this mechanism should occur but there is little evidence this happens at significant levels during sintering [2].
- (5) From the grain boundary to the neck.

- (6) From dislocation in the grain volume to the neck.

The driving force of volume diffusion is the difference in vacancy concentration in the grain. The concentration depends on the curvature of the surface [2, 8]. This is expressed in the following equation 2.2 [9]

$$C - C_o = -\frac{M\gamma_{sv}}{\rho R_c T}\left(\frac{1}{R}\right)C_o \tag{2.2}$$

With C the concentration of vacancy under a curved surface and C_o the equilibrium vacancy concentration. According to equation 2.2, a convex curved surface has a lower vacancy concentration than the equilibrium concentration. Alternately a concave curved surface has a higher vacancy concentration than the equilibrium. The vacancy concentration difference is the driving force of volume diffusion.

Grain boundary diffusion

The diffusion of atoms along the boundary between two particles is known as grain boundary diffusion. The atoms in a particle are orientated in one direction. If the orientations of the atoms in the two particles do not match, vacancies are created along the grain boundary, see Figure 2.2. These defects act as vacancies as described in volume diffusion. The atoms move from the grain boundary to the neck region.

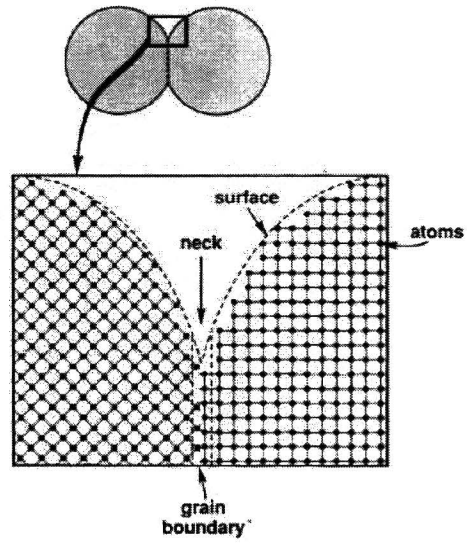

Figure 2.2: Misorientation at the grain boundary [2].

2.1.3 Viscous flow

Beside the six transport mechanisms that have been described for polycrystalline material, viscous flow describes the sintering process for amorphous material [10]. Amorphous materials have no melting temperature, but a melting trajectory. The viscosity of amorphous

materials decrease with an increasing temperature. The lower the viscosity the faster the sintering process occurs. The viscosity as function of temperature can be described with [2].

$$\eta = E\ exp\left(\frac{Q}{R_c T}\right) \tag{2.3}$$

With η the viscosity, E the pre-exponential constant and Q the activation energy. Glasses have a finite viscosity above the glass-transition temperature and are then capable of viscous flow [10], see figure 2.3. Example of materials that can be sintered by viscous flow are earthenware, sanitary ware, porcelain, glasses and also polymers [10]. The influence of the temperature on the viscous sintering process is shown in figure 2.4.

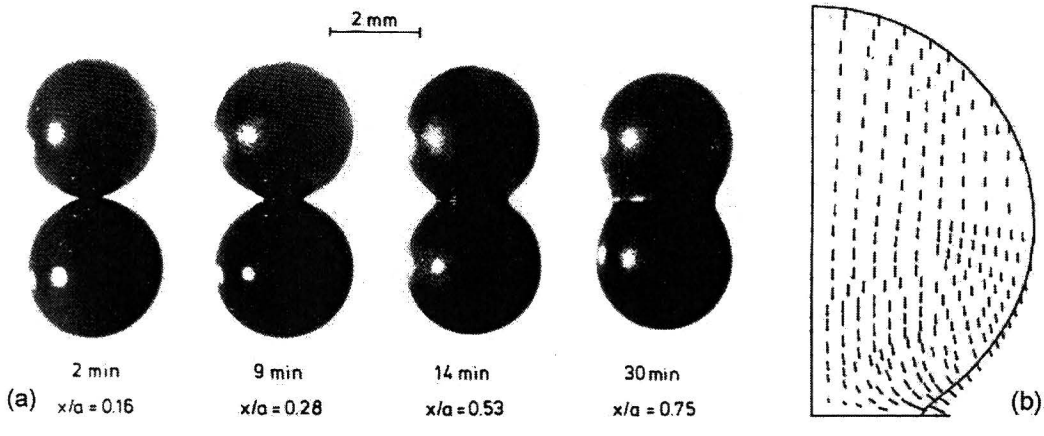

Figure 2.3: (a) Two-particle model of glass sphere sintered at 1000°C. x and a are respectively, the radius of the neck and the sphere [11]. (b) Mass flow during viscous sintering [6]

.

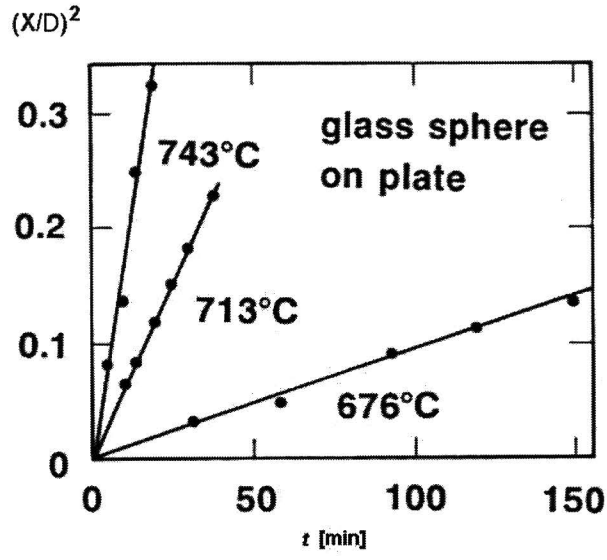

Figure 2.4: Viscous flow sintering data [2]. X/D is the ratio between the neck diameter and the particle diameter.

2.1.4 Liquid sintering

If a liquid is present during the sintering process, the capillary force drives the liquid in the narrow space between the contact point between the grains. This leads to high capillary pressure on the grain surface, which aids densification [2].

- Liquid sintering rearranges the particles to achieve better packing.
- Liquid sintering increases the contact pressure between particles, which is beneficial for the mass transport rate.

The capillary pressure can achieve a pressure 7 MPa or larger. The rate of liquid sintering is influenced by;

- Particle size
- Surface tension
- Viscosity

Smaller particles have a higher capillary pressure and surface energy than larger particles. The driving force for densification is larger for small particles. The amount of liquid increases with a rising temperature, which can be beneficial for the rate of densification or excessive grain growth (which reduce strength). The mass transport through a liquid is much faster than in solids [6]. The thickness of a liquid bridge between two grains is significantly larger than the grain boundary, which is also beneficial for mass transport [6].

2.2 Stages of Sintering

During the sintering process many material properties change. The material properties change at different temperatures and with different rates [5]. Sintering can be simplified by describing sintering in stages of physical changes, which occur in the transformation of a powder compact into a strong dense object. With this approach sintering can be described in three different stages.

- Initial stage
- Intermediate stage
- Final stage

Initial stage

The initial stage starts with a powder. The particles in the powder are pulled together by van der Waals forces (adhesion). The particles are randomly situated, which may imply misorientation at the contact point between the grains. The misorientation at the contact points cause rotation or movement of the particles [2]. The rearrangement increases the number of contact points to obtain a higher packing density and lower the surface energy [8]. At the contact points neck formation starts, see figure 2.5b. Mass transport from the surface of the grains to the neck regions leads to neck formation in the powder compact. The end of the initial stage is defined when the neck size ratio X/D reaches a value of 0.3 [2]

Intermediate Stage

At the end of the initial stage the grains are in contact with their nearest neighbors. The densification in the initial stage is only of minor level. In the intermediate stage the major part of the total densification occurs and most material properties of the final sintered compact are determined in this stage [2, 6].The neck size increases and the centers of the grains move closer together, which results in densification. The driving force in the intermediate stage is reducing the remaining surface energy. The spherical grains transform into a tetrakaidecahedra. With this structure it is possible to achieve full densification. In the intermediate stage the pores are located on the edges of the tetrakaidecahedra, see figure 2.5c. The pore network is still continuous. The pore shrinking continues in the intermediate stage until the pores become unstable and collapse, leaving isolated pores.

Final stage

In the final stage [6] the pores are isolated, see figure 2.5d. Final stage sintering is a slow process compared to the initial and intermediate stage. In the final stage some grains grow at the expense of others [12]. The mechanism that drives grain growth, is reducing the total grain boundary area. By reducing the grain boundary area the sintered compact reduces

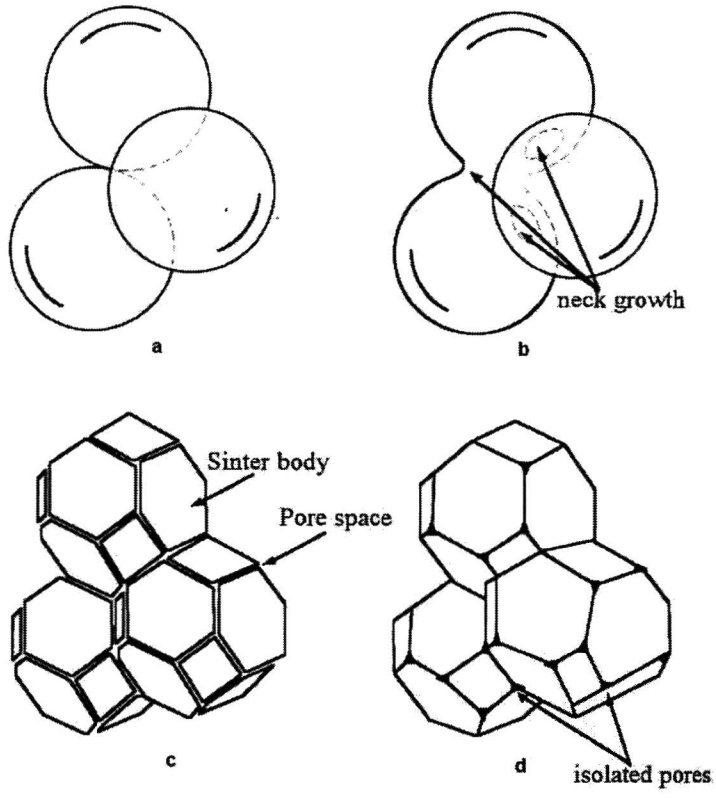

Figure 2.5: (a) The beginning of the initial stage. (b) The end of the initial stage; neck formation is begun (c) Intermediate stage; grain structure is tetrakaidecahedra, the pore are located on the edges. (d) Final stage; pores are located on the corners.

its energy. Grain boundaries can move to consume other grains. If the grain growth is faster than the pore mobility, the pores will be isolated inside the grain. This results in slower densification. If the pore mobility is larger than the grain growth the pores will move along the grain boundary and eventually disappear at the grain surface.

2.3 Analytical models

Frenkel was the first to develop an analytical model that describes the sintering process for viscous flow [13]. In the 1940s and 1950s, major contributions were made by Kuczynski [3], Kingery [14], Coble [9]. The analytical models describe the sintering process in a way that one transport mechanism is supposed to be the dominant. The geometry of the particles is simplified (spherical or cylindrical). For each stage (initial, intermediate and final stage) the analytical models are given below.

Initial stage

The initial stage model is a two-sphere model. The spheres are in contact with each other and are equal sized. The neck formation can occur with or without densification. The

neck is assumed to be circular. The grain boundary energy, which is responsible for grain growth, is neglected, because it is assumed that r is constat over the neck surface [6]. x and r are the two principals of curvature of the neck surface, see Figure 2.1. The equations for neck growth can be expressed in a general form [6].

$$\left(\frac{X}{D}\right)^m = \frac{H}{D^n}t \tag{2.4}$$

Here m and n are numerical exponents that depend on the mechanism of sintering. H is a function of material and geometrical parameters. X/D is the ratio of the neck diameter and the particle diameter (m, n, and H are given in Table 2.1). According to equation 2.4 a plot of $log(X/D)^m$ versus $log(t)$ yields a straight line. The value of m can be found to fit the theoretical equations to the experimental data. The value of m shows, which of the mechanisms is dominant. According to Rahaman [6] almost all studies reported excellent agreement between the theoretical predictions and the data. The problems can arise

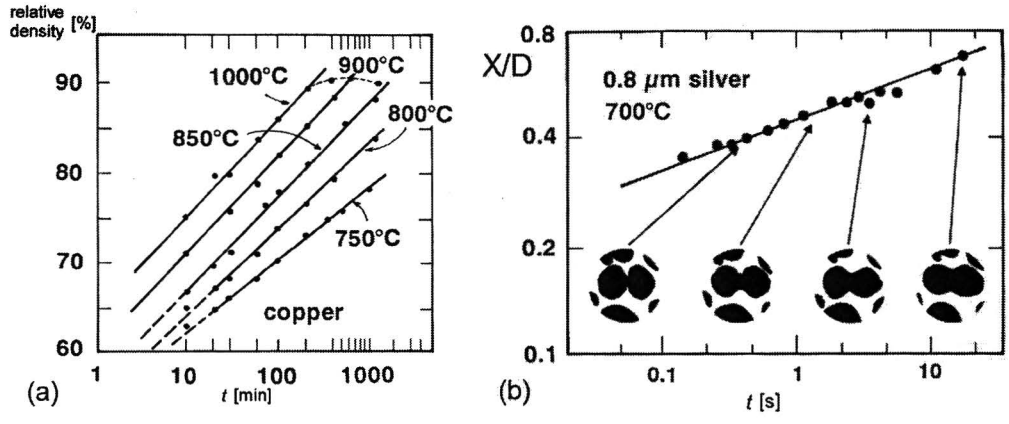

Figure 2.6: (a) Sintering of copper particles at different temperature. Densification rate increases with increasing temperature [2]. (b) Sintering of silver particles at 700°C [2].

when useful information is extracted from these plots. When more than one mechanism operates simultaneously, the interpretation of data can be misleading. For example, for copper sintering [2] the experimental data indicate that volume diffusion is the dominant transport mechanism, but detailed analysis indicates that surface diffusion is the dominant mechanism, with a significant contribution from volume diffusion. Although the model is not perfect it is important for understanding the initial stage of sintering [2]. Equation 2.4 illustrates some important processing parameters. A high sensitivity to the inverse particle size means that smaller particles cause more rapid sintering. In all cases, the temperature appears in an exponential term, meaning small temperature changes can have a large effect. Finally, time has a relatively small effect in comparison to temperature and particle size.

Table 2.1: Transport mechanism in the initial stage.

Symbols, δ_{sv}, δ_{gb} thickness surface and thickness grain boundary. γ_{sv}, surface energy. D_v, D_{gb}, D_s, diffusion coefficients for volume, grain boundary and surface diffusion. p_0, vapor pressure over a flat surface. m_a, mass of atom. b, burgers-vector. α , evaporation coefficient and Ω, volume of a atom.

Transport mechanism	m	n	H	
Surface Diffusion	7	4	$\frac{56\pi\delta_{sv}D_s\gamma_{sv}\Omega}{kT}$	$\left(\frac{X}{D}\right)^7 \sim t$
Vapor transport	3	2	$\left(\frac{3p_{vap}\gamma_{sv}}{\rho^2}\right)\left(\frac{\pi}{2}\right)^{\frac{1}{2}}\left(\frac{M}{R_cT}\right)^{\frac{3}{2}}$	$\left(\frac{X}{D}\right)^3 \sim t$
Grain boundary	6	4	$\frac{20\delta_{gb}D_{gb}\gamma_{sv}\Omega}{kT}$	$\left(\frac{X}{D}\right)^6 \sim t$
Volume diffusion	5	3	$\frac{80D_v\gamma_{sv}\Omega}{kT}$	$\left(\frac{X}{D}\right)^5 \sim t$
Plastic flow	2	1	$\frac{9\pi bD_s\gamma_{sv}}{kT}$	$\left(\frac{X}{D}\right)^2 \sim t$
Viscous flow	2	1	$\frac{3\gamma_{sv}}{\eta}$	$\left(\frac{X}{D}\right)^2 \sim t$

Intermediate stage models

In the intermediate stage most of the densification occurs. This stage is the most difficult stage to describe with analytical models [6]. Coble [9] made the following assumption to simplify the intermediate stage:

- The powder compact is composed of ideally packed tetrakaidecahedra of length l_p, each tetrakaidecahedra represents one grain.
- The pores are cylindrical and are positioned at the edges of the tetrakaidecahedra
- The vacancy concentration is linear between the source and the sink. Grain boundary acts as vacancy sinks
- Surface transport mechanisms don't share in the mass transport, because the chemical potential of the pore is everywhere the same.

With these assumptions Coble derived the following equation for volume diffusion [6].;

$$P_c \approx \frac{r^2}{l_p^2} \approx \frac{10D_v\gamma_{sv}\Omega}{l_p^2kT}(t - t_f) \tag{2.5}$$

And for grain boundary diffusion;

$$P_c \approx \frac{r^2}{l_p^2} \approx \frac{2D_{gb}\gamma_{gb}\Omega}{l_p^4kT}t^{2/3} \tag{2.6}$$

With r the radius of the cylindrical pore and t_f the time the pores are vanished. The model is valid until the pores collapse into spherical pores. The equations can only be considered as an order of magnitude calculation, because of the many assumptions made in the model [6].

For amorphous material in the intermediate stage, Scherer [15] made a model of a cubic array formed by intersecting cylinders, which describes viscous sintering. Densification occurs by decreasing the length of the cylinder and increasing the radius of the cylinder. The following viscous sintering equation can be derived. The equation describes the density

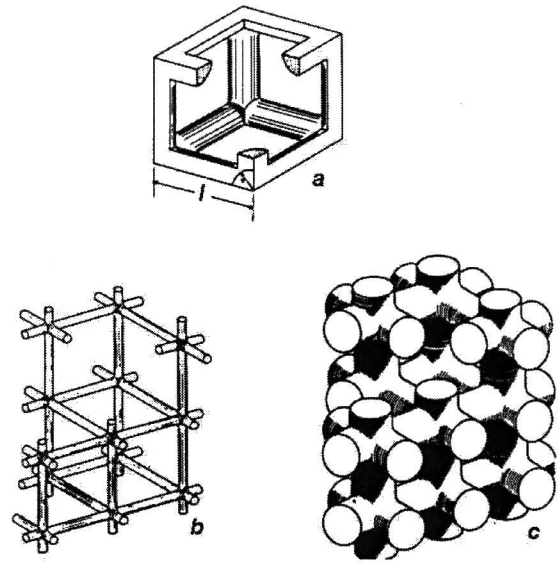

Figure 2.7: Unit cell with edge length l and cylinder radius a. (b) Microstructure with a relative density of 0.1. (c) Microstructure with a relative density of 0.5 [15]

change as function of time for a specify temperature.

$$\frac{\gamma_{sv} N^{1/3}}{\eta}(t - t_o) = F_s(y) - F_s(y_o) \tag{2.7}$$

$$F_s(y) = -\frac{2}{\alpha}\left(\frac{1}{2}\ln\left(\frac{\alpha^2 - \alpha y + y^2}{(\alpha + y)^2}\right) + \sqrt{3}\arctan\frac{2y - \alpha}{\alpha\sqrt{3}}\right) \tag{2.8}$$

With t_o the time when the intermediate stage starts, y a function of the density, N the numbers of pores per cubic meter and $\alpha = (8\sqrt{2})^{1/3}$. Despite of the simplifications this equation is valid for a wide density range [6], see figure 2.8b.

Final stage

Coble's final stage model [9] describes a powder system of equal-sized tetrakaidecahedra. In the final stage the pores are located on the 24 corners of the tetrakaidecahedron. Each pore is connected to four grains. The final stage model can be derived similar to the intermediate stages models. The volume diffusion grain boundary can be expressed as.

$$P = \frac{6\pi}{\sqrt{2}}\left(\frac{D_l \gamma_{sv} \Omega}{D^3 kT}\right)(t - t_f) \tag{2.9}$$

with P the porosity and t_f the time when the pore vanishes. This equation is supposed to be valid for a porosity less than 2% [6]. For amorphous material in the final stage of sintering Mackenzie and Shuttleworth derived the following expression [15], see figure 2.8b.

$$\frac{\gamma_{sv} N^{1/3} t}{\eta} = F_{ms}(\rho) - F_{ms}(\rho_0) \tag{2.10}$$

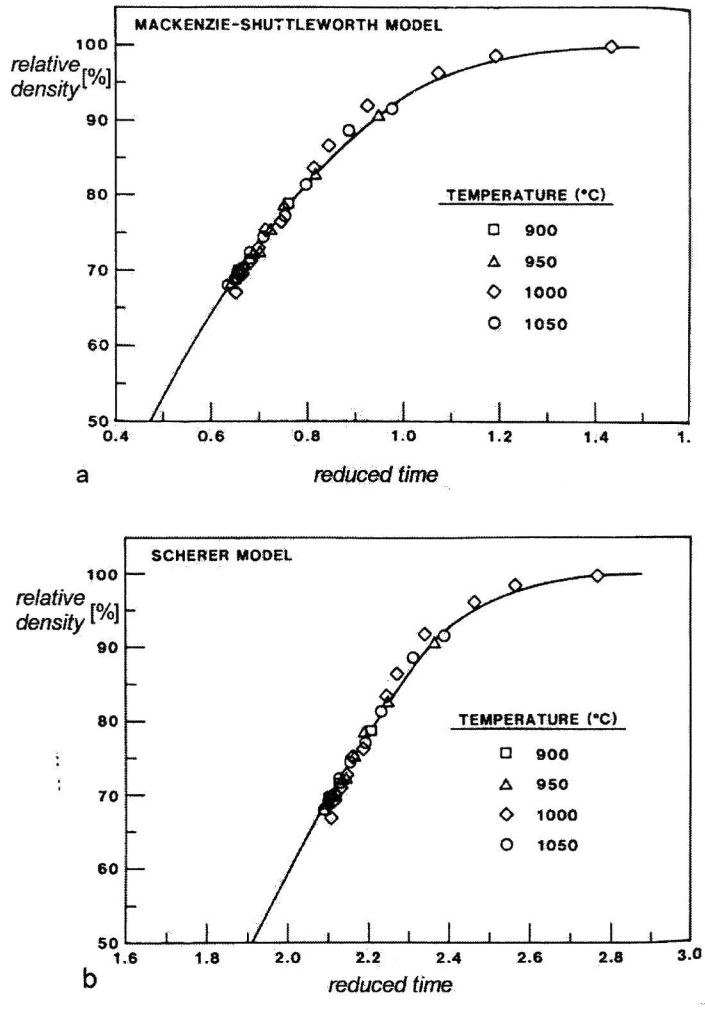

Figure 2.8: (a) Viscous model for final stage. (b) Viscous model for intermediate stage. Data experiments of sintered glass. With $\frac{\gamma_{sv} N^{1/3}}{\eta}(t - t_o)$ the reducing time.

$$F_{ms}(\rho) = \frac{2}{3}\left(\frac{3}{4\pi}\right)^{1/3}\left(\frac{1}{2}\ln\left(\frac{1+\rho^3}{(1+\rho)^3}\right) - \sqrt{3}\arctan\frac{2\rho-1}{\sqrt{3}}\right) \tag{2.11}$$

The analytical models that are developed in the 1940s and 1950s have given a great understanding of the sintering phenomenon. The initial stage model can be described with the most accuracy compared to the other stages. The simplifications made with respect to the geometry are too drastic to be able to describe the sintering process accurately [6].

2.4 Numerical Models

In view of the drastic simplification made in the analytical models, attempts have been made to use numerical simulation to provide a better description of some of the complexities of sintering, such as more realistic neck geometries and the occurrence of simultaneous mechanisms [6]. In the 1970s the first sophisticated models were developed, based on less

simplified pore geometries and taking superposition of various sintering mechanisms into account [16]. Similar to the analytical models the numerical models describe sintering mechanism in stages (initial stage, intermediate stage, final stage) [2]. The introduction of numerical methods helped dealing with more realistic situations. For example, finite element simulations in combination with macroscopic continuum models allow quantitative predictions of the sintering process. The driving force in the continuum models is the sintering stress. The sintering stress depends on the density, surface tension and particle size. Another approach to model sintering is making use of Monte Carlo simulations [17]. Monte Carlo can be used for modelling microscopic formation, diffusion, and annihilation of vacancies [17]. The great challenge in the modelling of sintering is to connect the micro- and macroscopic models together. The table below lists several report about numerical models.

Table 2.2: Overview of several computer simulations of solid-state sintering.
GB = grain boundary diffusion, VD = volume diffusion, SD = surface diffusion, VS = Viscous flow, CT = continuum theory, MC = Monte Carlo and SP = Stokes problem.

Mechanism	Based on	Include	Reference
GB	CT	Densification, grain growth	[18]
GB	CT	Densification, particle size distr.	[19]
GB + VD + SD	CT	Densification	[16]
VS	CT	Densification	[20]
VS	CT	Densification	[21]
Multiple	MC + CT	Densification	[17]
GB	MC	Densification	[22]
VS	SP	Densification	[23]

Although much progress have been made in modelling of sintering using numerical models. Modelling of practical realities as nonlinear heating, wide particle size distribution, liquid formation, atmosphere interactions are still hard to accomplish [2].

2.5 Minimum sintering temperature

To start the sintering process a certain minimum temperature is needed [24]. This temperature, called minimum sintering temperature T_s, is necessary to exceed the activation energy, which holds the atoms together. The minimum sintering temperature is material [25, 26, 27] and particle size dependent [2, 24].

Table 2.5 shows the minimum sintering temperature for some materials and particle diameters. The minimum sintering temperature is usually measured with dilatometry. A dilatometer measures the expansion or shrinking of a material. A typical dilatometry curve is shown in figure 2.9. ΔL is the dimension change of the material. The minimum sintering temperature is defined as the point where $dL/dT = 0$. The thermal expansion cause an increase in ΔL for the first part of the curve. From the point T_s sintering overrules the thermal expansion and causes the material to shrink. Other techniques that can be used

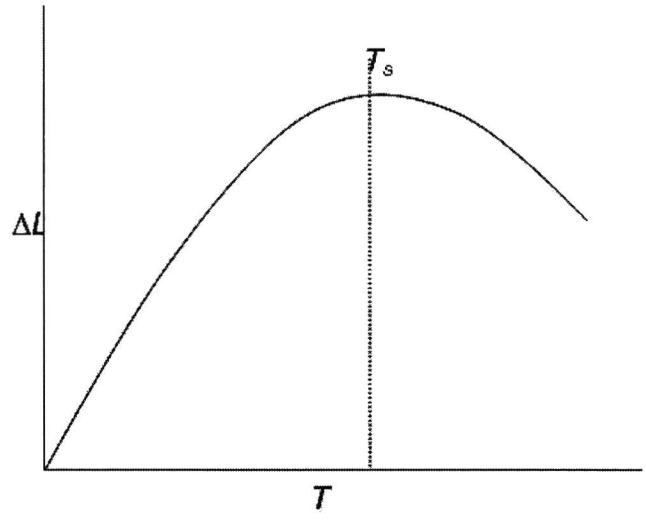

Figure 2.9: A typical dilatometer curve for determining the minimum sintering temperature.

for determination of the minimum sintering temperature the reader is referred to [29].

Table 2.4: Minimum sintering temperature for coal ash.

D_p the average particle diameter		
Particle size range [mm]	D_p [mm]	T_s [°C]
1-3	1.9	930
1-1.4	1.1	810
0.7-1.4	1.0	800
0.7-1.0	0.8	720
0.5-1.0	0.75	700
0.5-0.7	0.65	695

T_s decreases with a decrease in particle size. The influence of the particle diameter is demonstrated for coal ash by Basu [28], see table 2.4. Other examples of influence of the particle size on sintering process are given in figures 2.10a-b. The figures show the relationship between particle size and density with a constant sintering temperature and a constant sintering time. The smaller the particle size the faster the sintering process proceeds.

Table 2.3: Minimum sintering temperature for different materials.
D_p is the mean particle diameter, ρ is the theoretical density, $\dot{Q}$ is the heating rate, T_s minimum sintering temperature and T_m is the melting temperature.

Material	D_p [μm]	$\dot{Q}$ [$\frac{°C}{min}$]	T_s [°C]	T_m [°C]	$\frac{T_s}{T_m}$ [–]
Calcium chloride	500	10	440	773	0.57
Sodium chloride	359	3.33	463	800	0.58
Sodium bromide	359	3.33	480	755	0.64
Sodium citrate	359	3.33	203	310	0.65
Aluminum sulfate	150	10	340	770	0.44
Magnesium sulfate	-	10	524	1124	0.47
Ammonium chloride	359	3.33	245	350	0.70
Glass beads	718	4	589	-	-
Glass beads	275	4	585	-	-
North Dakota lignite coal ash	-	3.33	574	-	-
Illinois 6 coal ash	-	3.33	798	-	-

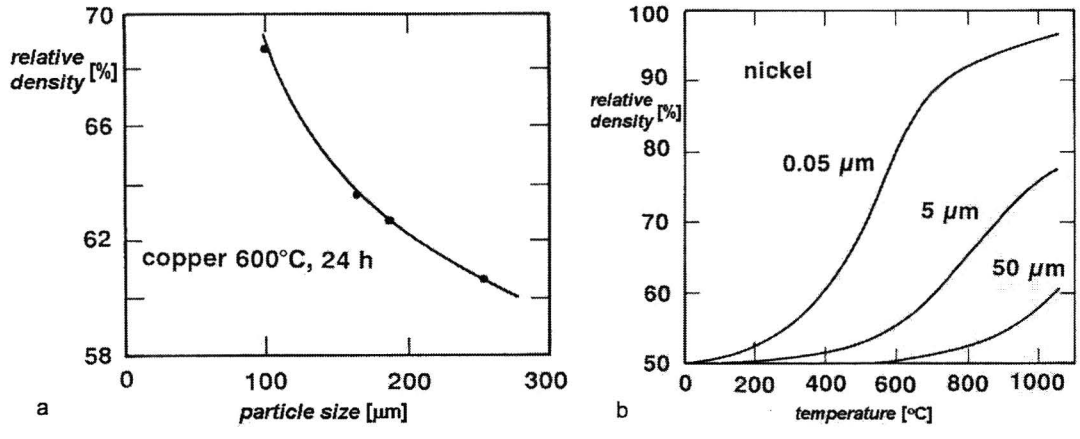

Figure 2.10: Influence of the particle size on the densification rate [2]. (a) Sintering of different size copper particle with constant sintering time and temperature. (b) Sintering of three different Nickel particles plot in a temperature versus relative density diagram.

Skrifvars et al [25, 26, 27] measured for 14 different biomass ashes the minimum sintering temperature in a range between 600-1000 °C, and for 12 different coal ashes in a range between 500-900 °C.

2.6 Sintering measurement techniques

In "Sintering theory and practice"German [2] describes several measurement techniques for quantifying the sintering process. Parameters that are relatively easy to measure are density, porosity, grain size, neck size, and pore size (with stereology).

Density and porosity

For a porous structure the relative density is mostly given in stead of the density. The relative density is the ratio between the density of the porous structure and of a solid. The relation between relative density and porosity can be stated as followed.

$$\rho_r + P = 1 \tag{2.12}$$

With ρ_r the relative density, P the porosity. Several measurement technique for measuring the porosity and density will be given.

- The density of a porous structure can be measured with the Archimedes technique. This technique is only suitable for materials that do not dissolve in the fluid. The fluids commonly used are water, silicone or paraffin oil. This method is only suitable for open pores. According to German [2] the pores are open up to a density of 92 %.

- For complex geometries gas pycnometry can be used. The sample is place in the vacuum chamber of the pycnometer. A gas (usually helium) will be pumped into the chamber. The change of the pressure is a measure for the volume displacement. Helium is a one-atomic inert gas with a very small particle diameter and therefore suitable as a measurement gas. It can penetrate more effectively in the existing structures.

- Another technique to determine the porosity, pore-size and volume is called Mercury Porosimetry. This technique provides measurements of pore radii from cm to nm. Using the principle that a force or pressure is needed to fill a pore. The porosity can be calculated by measuring this force and the volume of intruded liquid in the porous material.

- Microscopic analysis and point counting techniques can be used for determining the porosity. If the porosity is randomly distributed, the porosity of the 2D image is equal to the volume porosity (Delesse's principle [30]).

The porosity measurement with microscopic analysis and point counting techniques will now be described in more detail. The surface porosity of the sample cannot be visualized straightaway, the sample must first be prepared. The sample is placed in epoxy and in a oven for 2h at 80°C. By heating the epoxy it will transform into a solid. Finally the sample must be polished and can be placed under the SEM (scanning electron microscope). Figure 2.11a shows a SEM image of a fouling layer and figure 2.11b shows the same image as only it is transformed into a black and white image. The luminance values of the pixels in figure 2.11a span from 0 (black) to 255 (white) with the darker pixels corresponding to void space and the lighter pixels corresponding to particles. A threshold within this range must be defined to differentiate between solid and void space. This threshold was defined using the histogram minimization method [42], see figure 2.12. The porosity can be determined by calculating the percentage of black pixels.

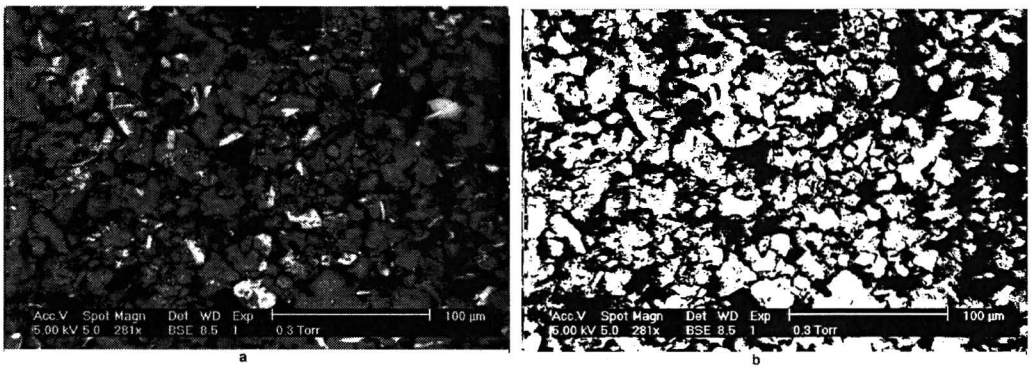

Figure 2.11: (a) Polished fouling, (b) black and white image.

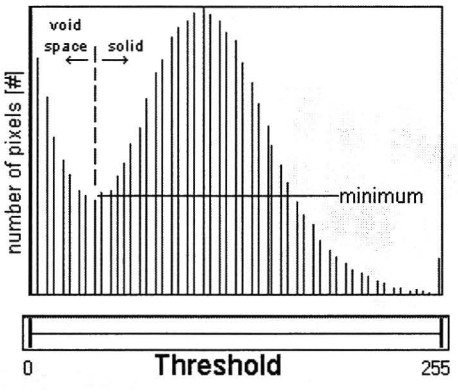

Figure 2.12: Threshold histogram used for determination of the threshold between the solid and void spaces.

Strength

The porosity of a sample influencing the strength of the sample [31]. The lower the porosity the higher the tensile or compression strength. Several methods that measures the strength [31] are available, like tensile strength test, compression strength test and impaction test.

Neck size

The neck size give an indication of the degree of sintering. The neck size for spherical neck area's can be measured by zooming in on the neck between two particles with the SEM-analysis. With a tool inside the SEM-software the neck can be measured as shown in figure 2.13

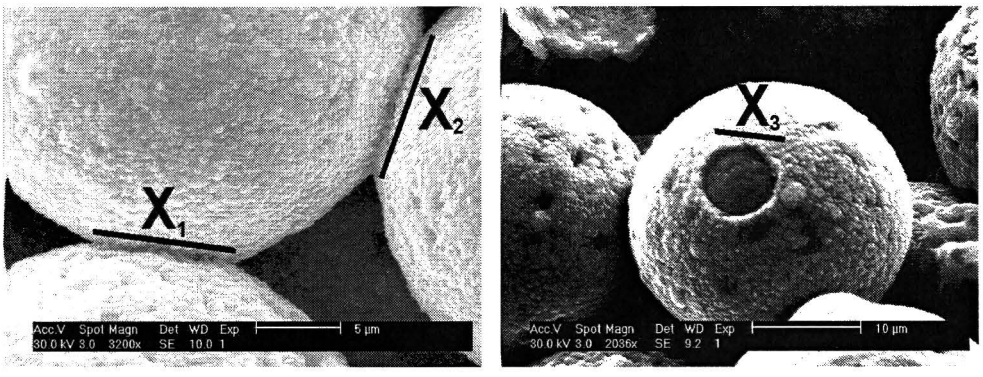

(a) (b)

Figure 2.13: Shows the measurement method in which the neck sizes are measured.

Sintering kinetics

Pressure-Drop Sintering Technique (PDS) has been developed to determine the sintering rate of coal ash based on the measurement of the pressure-drop across a pellet of ash. The technique monitors the changes in porosity as a function of time, which is an indication of the degree of strength development due to sintering [32].

Chapter 3

Experimental methods

Experiments are set up to study the influence of sintering on fouling of heat exchangers. In section 3.1 the influence of the sintering process on particle deposition and particle removal is studied Impaction experiments are conducted to measure the sticking, rebound and removal behavior as a function of the impact speed. An experiment is set up to determine the effect of a temperature gradient on a fouling layer. In heat recovery system a temperature gradient is established between the top and bottom of a fouling layer, due to the hot flue gasses and the relatively cold heat exchanger tube. Therefore an experiment is set-up to see the influence on the fouling layer structure when the temperatures in the temperature gradient exceed the minimum sintering temperature. From a biomass gasifier fouling layer material is taken to determine the minimum sintering temperature. Conclusion are be drawn when the minimum sintering temperature is compared with the gas-side temperature in the gas cooler itself, see section 3.3

3.1 Impaction experiments

3.1.1 Description of the set-up

The experimental set-up consists of a vacuum column mounted on a vacuum chamber. In the vacuum column a particle feeder is placed. The particle feeder allows the incident particles to be dropped in a controlled way. The height of the column and pressure inside the column can be changed yielding to a maximum impact velocity of 4 m/s for a column height of 1 m. After being released from the particle feeder, the particles fall through the column and impact on a sample that is installed in the vacuum chamber on a object table. The impacts are recorded with a digital, see figure 3.2. The camera used (JAI CV-M10) has a frame rate of 30 frame/s. The images have a maximum resolution of 512 x 512 pixels and images are stored in a framegrabber. To be able to measure the velocities of the particles a continuous 5W argon-ion laser beam is pulsated by an optical chopper with a maximum chopping frequency of 5000 Hz. The laser beam is directed through a cylindrical lens to create a light sheet with a thickness of 2 mm. A particle that falls in the light sheet is recorded. For the recorded impaction the impact velocity, rebound velocity, rebound

angle and energy loss is measured, see figure 3.1a. The incident particles hit a sintered sample with particles with known particle and neck sizes. The diameter of the incident particles are similar to the particles in the sintered sample.

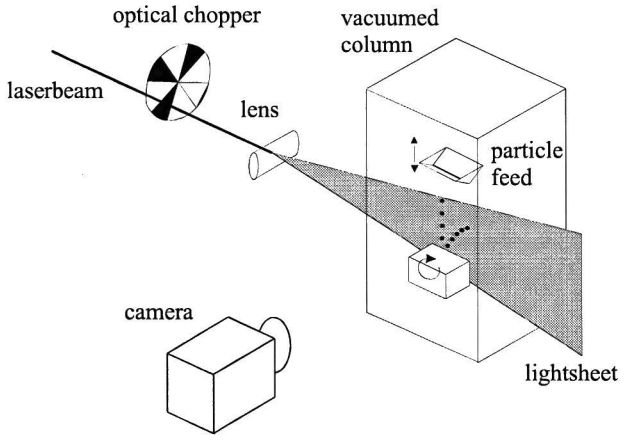

Figure 3.1: Schematic representation of the camera system in

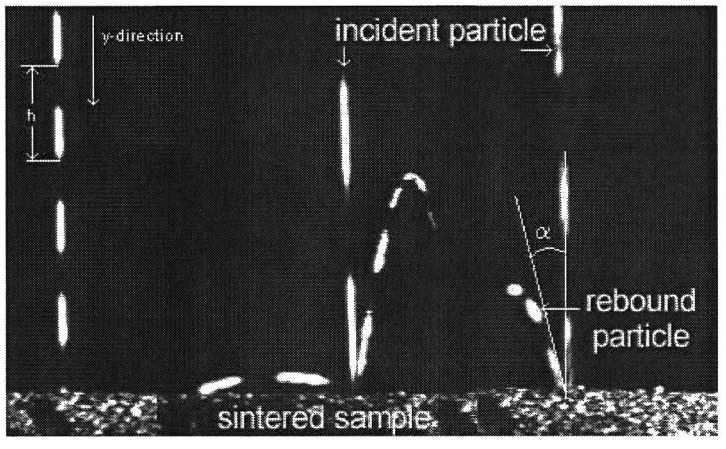

Figure 3.2: A typical image that captures the impacts, (left) sticking, (middle) removal, (right) one rebound. With α the rebound angle.

3.1.2 Data analysis

Particle velocity

The velocity of a particle can be determined from the distance between two successive illuminations (blobs), see figure 3.2. The velocity is found from:

$$v_i = \frac{h}{c} f_{ch} \tag{3.1}$$

With, v_i the impact velocity, h the distance between two blobs (in pixels), c the numbers of pixels per meter and f_{ch} the chopper frequency. h is manually measured with the software

programme Imagetool version 3.00. A reference object is placed in the middle of the laser sheet and the camera is focussed on the reference object. The reference object consists of millimeter paper, an image token from this object is used as calibration image. From the calibration image c can be measured.

Rebound angle

The rebound angle α is determined using the software program Imagetool. The angle can be determine by drawing lines for the incident and rebound path, see figure 3.2. The rebound angle is measured within 0.25° accuracy.

3.1.3 Error analysis

In the experiments the velocities are calculated from independent quantities such as the chopper frequency, the distance between the blobs and the dimension of the camera, see table 3.1. For a more detailed description of the error analysis the reader is referred to [1].

Table 3.1: Random errors for the measured quantities

Quantity	Symbol	Error
Chopper frequency	f_{ch}	0.5%
Distances	h, H and c	1 pixel

3.1.4 Sample preparation

For the analysis of the experiments it is important to have a well defined sample and incident particles. For the impaction and temperature gradient experiment spherical bronze particles are used. The particles are sieved with cut-off sizes 25 and 32 μm (batch 1) and are sieved with cut-off sizes 50 and 56 μm (batch 2). The particle size distribution of the obtained particle fractions is measured using a Coulter particle sizer, see Appendix A.

3.1.5 Experimental procedure

The sieved bronze particles (batch 1) are placed in a stainless steel sample holder. Tapping the sample holder ensures a more uniform distributed porosity throughout the sample. The samples are placed for 1h, 6h and 48h in a hot air oven at 200 °C. After taking the samples out of the oven the neck sizes are determined using SEM-analysis, see figure 2.13. Additional samples are made in a tube-oven filled with nitrogen to ensure the bronze particles will not oxidize. The bronze particles (batch 2) are placed in the tube-oven at 500 °C for 5h and 20h.
After this procedure the samples are placed one at a time on a table in the vacuum chamber. The laser sheet is aligned with the plane in which the particles fall. Particles are dropped on the sample. The speed of the incident particles is controlled by changing the height

of the column or the pressure inside the column. The recorded impacts are analyzed on sticking, rebound and removal. Sticking is the deposition of particles after impacting on a surface. Removal occurs when an incident particle hits a fouling layer with enough energy to break the existing bonding between the particles in the sintered surface and remove one or more particle(s) out of the surface.

3.2 Temperature gradient experiments

3.2.1 Description of the set-up

The temperature gradient experiment consists of an oven and a cooling channel. The temperature difference between the top and bottom of the powder is established by heating the top with a controlled electric ceramic heater and the bottom is cooled with a cooling channel with a constant water flow. A schematical representation of the set-up is given in figure 3.3a, see also appendix B. The set-up consists of an oven and a cooling channel. The oven consists of an electric ceramic heater (type: SHTS Elstein) surrounded by high temperature insulating board. The heater is capable of reaching a maximum temperature of 900 °C with a heat output of 800W. The heater is controlled by a control unit (type: TRD Elstein). The bottom of the oven has a rectangular opening, which fits the sample holder. The sample holder is glued onto the cooling channel and is made of high temperature insulating board. The middle of the sample holder can be filled with powder. The box-shape cooling channel has two in and outlet tubes and can be connected to the water grid. The temperatures are measured on the top and bottom of the sample, respectively T_t and T_b. The water temperatures are measured before entering and after leaving the cooling channel, respectively $T_{w_{in}}$ and $T_{w_{out}}$, see figure 3.3b. The temperature are measured with k-type thermocouples, which are connected to a temperature measurement card (NI4350) and to a computer for data logging.

3.2.2 Data analysis

Porosity

The bottom temperature of the sample is lower than the minimum sintering temperature, therefore a part with thickness s will sintered, see figure 3.3b. The porosity is determined by imbedding the sintered part in epoxy, cross section and polishing the sample for SEM analysis. The SEM makes images with a dark background of epoxy and light grey colored imbedded particles. By transforming the image into a black and white image, where the particles are white and the epoxy is black, the porosity can be determined by counting the amount of black pixels in the image. A typical SEM image is shown in figure 3.4. The measured surface porosity can represent a volume porosity, according to Delesse's principal [30], if the porosity is randomly distributed.

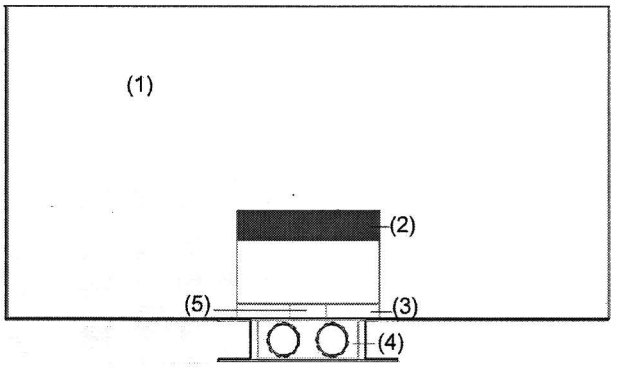

(a)

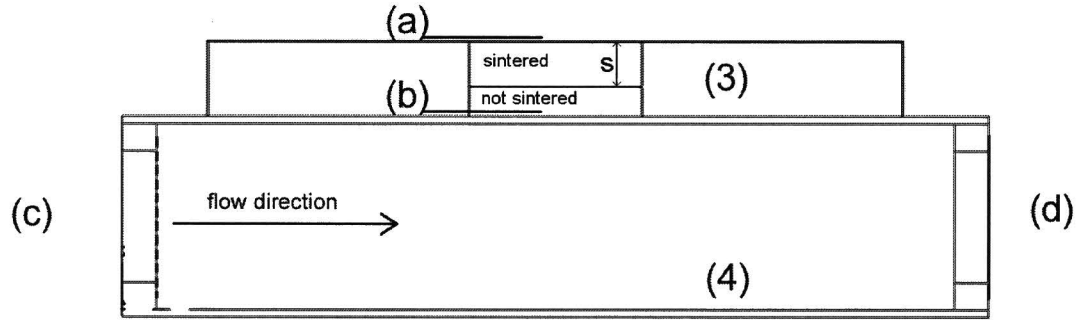

(b)

Figure 3.3: (a) A schematical representation of the set-up, with (1) high temperature insulating board, (2) ceramic heater, (3) sample holder, (4) cooling channel, (5) sample. (b) A schematic view of the cooling channel and the sample holder, with (a) top temperature T_t of the sample, (b) bottom temperature T_b of the sample, (c) water inlet temperature $T_{w_{in}}$, (d) water outlet temperature $T_{w_{out}}$

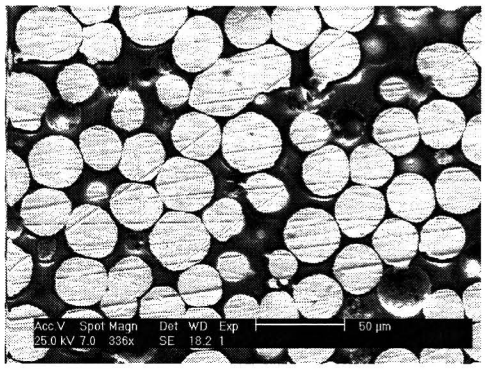

Figure 3.4: SEM image of a polished bronze sample

Mass flow

The water grid ensures that a constant mass flow passes through the cooling canal. The flow rate is measured by collecting several times the water from the exit tube for two minutes and measuring the weight of the water on a balance.

Thermal conductivity

The thermal conductivity cannot directly be measured, but can be estimated by.

$$Q_w = \dot{m} c_p (T_{w_{out}} - T_{w_{in}}) \tag{3.2}$$

With Q_w the heat transfer rate into the water, $\dot{m}$ the mass flow and c_p the specific heat of the water. The thermal conductivity of the powder (k_b = 10-20 W/mK) is much larger than the thermal conductivity of the sample holder (k = 0.20 W/mK). Therefore the heat transfer rate to water can be set equal to the heat transfer rate through the sample.

$$Q_w = Q_s = kA\frac{\Delta T}{\Delta x} \tag{3.3}$$

With k the average thermal conductivity of the sample, A the area covered by the sample, Δx the height of the sample and $\Delta T = T_t - T_b$.
so k is,

$$k = \frac{Q_w \Delta x}{A \Delta T} \tag{3.4}$$

3.2.3 Error analysis

Temperature

According to the specification of National Instruments all the temperature measurements with k-type thermocouples in combination with a NI4350 temperature card have an accuracy of 0.7 K. The control unit controls the temperature of the ceramic heater with a fluctuation of ± 7 K around the set-point. This fluctuation is also seen in the top temperature of the sample, with an amplitude of ± 2 K.

Porosity

The surface porosity is determined by averaging the porosities of ten images in a specific region, a scattering of ± 10% around the average value is typical.

Mass flow

The water from the exit tube is collected for 120 seconds. The collecting time is accurate within one second and the balance used for measuring the weight is 5 grams accurate.

Thermal conductivity

The accuracy of thermal conductivity depends on the temperature difference between $T_{w_{out}}$ and $T_{w_{in}}$, and the mass flow measurement. The temperature difference varies between 0.5 and 2 °C. The small temperature difference is in the same order as the inaccuracy of the thermocouples (1.4 °C). Although a trend in the change of the thermal conductivity within time can be measured.

3.2.4 Experimental procedure

The sample holder is filled with bronze particles (batch 1) until the thermocouple T_t is covered with particles. The oven is placed over the sample holder and on top of the cooling channel. The set-point of the ceramic heater is 400 °C, to ensure that the temperature in the oven is above the minimum sintering temperature. The temperatures T_t, T_b, $T_{w_{in}}$ and $T_{w_{out}}$ are measured to be able to calculate the change in the thermal conductivity within time. The water flow is controlled by adjusting the tap of the water grid.
If the bottom temperature is lower than the minimum sintering temperature, due to the cooling only a part with thickness s will sintered, see figure 3.3b. The thickness of the sintered part is dependent on the location of the minimum sintering temperature. The thickness of the sintered part is measured using a vernier calliper.

3.3 Minimum sintering temperature

3.3.1 Description of the set-up

An experiment is conducted to measure the minimum sintering temperature for fouling layer material and flyashes originating from a biomass gasifier. The fly ashes are collected after the gascooler in a cyclone. For the determination of the minimum sintering temperature an airtight aluminium oxide container is necessary to prevent oxidation and diffusion of vapors. The container is placed in a hot air oven at different temperatures.

3.3.2 Experimental procedure

The fouling layer is crushed into particles with a particle size smaller 56 μm, this resembles the particle size found for the particles in the fly ashes. The aluminium oxide container is filled with the flyashes or fouling layer material and is covered with an aluminium oxide plate. The plate is glued to the cup to ensure the container is airtight. Samples are placed for 20h at 675, 750 and 800 °C. After the experiment the samples are examined with SEM-analysis. The SEM is used to visualize the particle agglomeration.

Chapter 4

Experimental results

Experiments have been carried out to determine the influence of sintering on fouling. In this chapter the experimental results are presented for the experiments, that are described in the previous chapter. In section 4.1 the results of impaction experiments are presented. These impaction experiments show the effect of sintering on particle sticking and particle removal. The results of impaction experiments on a sintered surface are compared with the impaction experiments on a powdery surface [1, 33, 34, 35].
In section 4.2 a temperature gradient experiment is set up to determine the influence of a temperature gradient on the structure of a powder. The porosity of the layer and thermal conductivity are measured to study the change in the structure.
In section 4.3 is for a fouling layer, taken out of a gas cooler of a biomass gasifier, the porosity determined and the minimum sintering temperature measured and compared with the gas-side temperature in the gas cooler.
The observations made for different experimental results are discussed in section 4.4.

4.1 Impaction experiments

To determine the influence of sintering on particles sticking and particles removal, impaction experiments are conducted. Four different bronze samples are used for the impaction experiments, see table 4.1. Three bronze sample are sintered in a hot air oven at 200 °C for respectively 1, 6 and 48h. One sample is sintered at 500 °C for 20h in a tube oven filled with N_2 to prevent oxidation of the bronze particles.

Table 4.1: sample properties

Sample name	Environment	Sintering time [h]	Sintering temperature [°C]	X/D [-]
1h-sample	air	1	200	0.07
6h-sample	air	6	200	0.17
48h-sample	air	48	200	0.31
N2-sample	nitrogen	20	500	0.23

In subsection 4.1.1 the experimental results are discussed with respect to sticking, one

rebound and one particle removed from the impacted surface. Figure 3.2 shows the three different situations.
In subsection 4.1.2 the coefficient of restitution is presented for the 48h-sample and N_2-sample. The coefficient of restitution is a measure for the energy loses during an incident particle impact. The coefficient of restitution is defined as the ratio between the rebound velocity v_r and incident velocity v_i. Finally in subsection 4.1.3 a frequency distribution for rebound angles is given. A model is presented which describes the observed distribution.

4.1.1 Sticking and removal

In figure 4.1 the results of the impaction on the sintered bronze samples are plotted. The figures show the impaction speed versus sticking, one particle ejected, two particles ejected for the different samples. The experimental data from the impaction experiments are plotted in Appendix C. The figures in the appendix present the numbers of experiments versus impact speed for sticking, rebound or removal for 1h-sample, 6h-sample and 48h-sample. A low amount of data is found for removal of particles in the 48h-sample in comparison with the other samples. Therefore in figure 4.1c the line that describes two particles ejected is dashed.

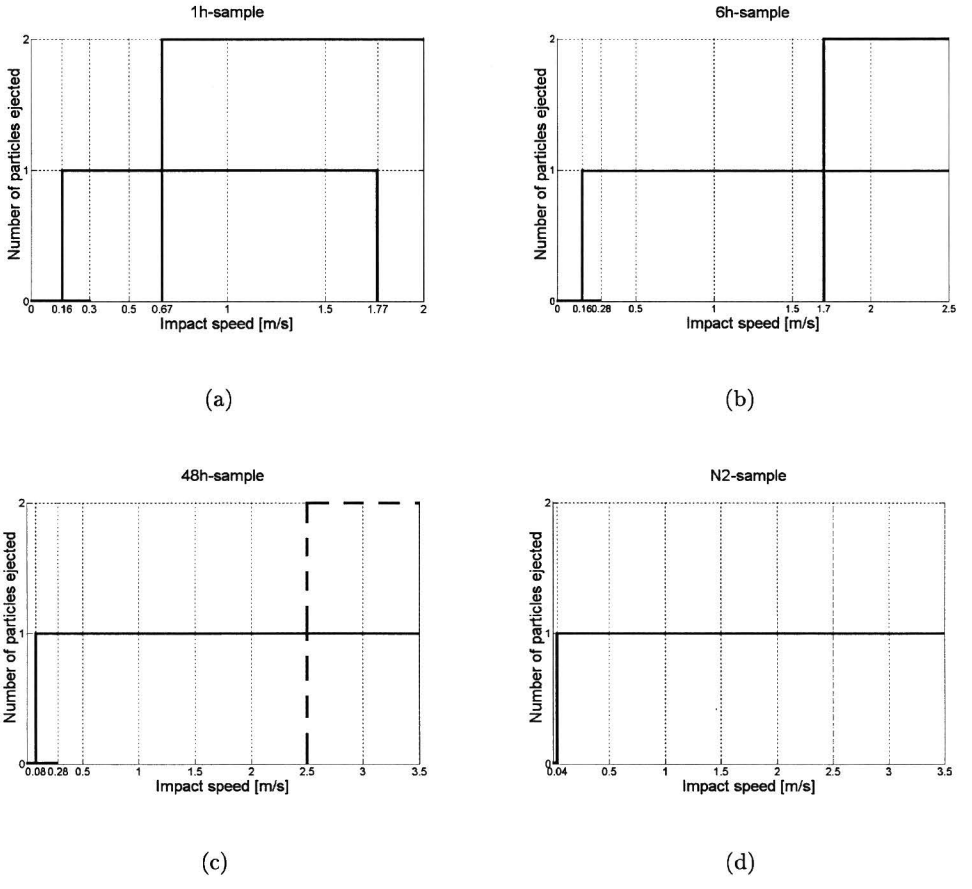

Figure 4.1: Number of particles ejected versus impact speed for different samples

Sticking

A significant difference can be found for the maximum sticking velocity between the sintered bronze samples in air and the sintered bronze sample in nitrogen. For the sintered bronze samples in air the maximum sticking velocity is nearly constant, approximately 0.3 m/s. For the sintered bronze sample in nitrogen the maximum sticking velocity is < 0.04 m/s.

One rebound

A rebound occurs when the incident particle leaves the surface after an impact. The minimum rebound speed is lower for the 48h-sample than for the 1h-sample, see figures 4.1a and c. The minimum rebound speed is for the 1h-sample 0.16 m/s and for the 48h-sample is 0.08 m/s. Figure 4.1d shows for the N2-sample a minimum rebound speed of 0.04 m/s, which is significant lower than the other samples.
Only for the 1h-sample a limit (1.77 m/s) is found where above only particle removal occurs.

Particle removal

The minimum velocity at which the incident particles can remove particles from the impacted surface increases for samples with higher degrees of sintering. For the 1h-sample a minimum speed of 0.67 m/s is found. For the 6h-sample and 48h-sample an impact speed of respectively 1.7 m/s and 2.5 m/s is required to start particle removal. Finally, no particle removal is observed for N2-sample .

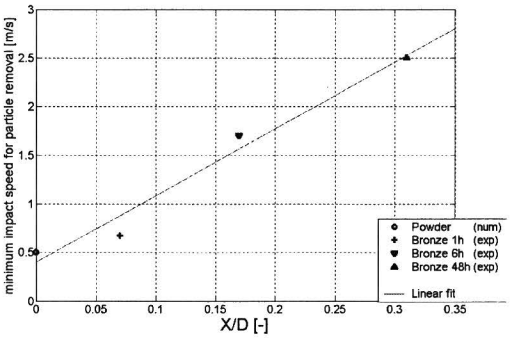

Figure 4.2: A plot of X/D versus the minimum speed removal speed. A linear fit is drawn through the experimental results

Figure 4.2 shows X/D versus the minimum removal speed. Point $X/D = 0$ represents a powdery sample, which is calculated using the numerical model developed by Abd-Elhady et al. [35]. A 'linear' behavior is observed.

4.1.2 Coefficient of restitution

During an impact kinetic energy will be lost due to elastic wave propagation, plastic deformation, electrostatic charges and adhesion [1]. The rebound velocity is therefore always

lower than the impact velocity. A measure for the energy losses during an impact is the coefficient of restitution. The coefficient of restitution is defined as

$$e = \frac{v_r}{v_i} \tag{4.1}$$

The coefficient of restitution versus the impact speed for the 48h-sample and the N2-sample are given in figures 4.3a-b. In figure 4.3 data is presented for impacts where only one rebound occurs. The scattering in figures 4.3a-b show a decrease in the maximum

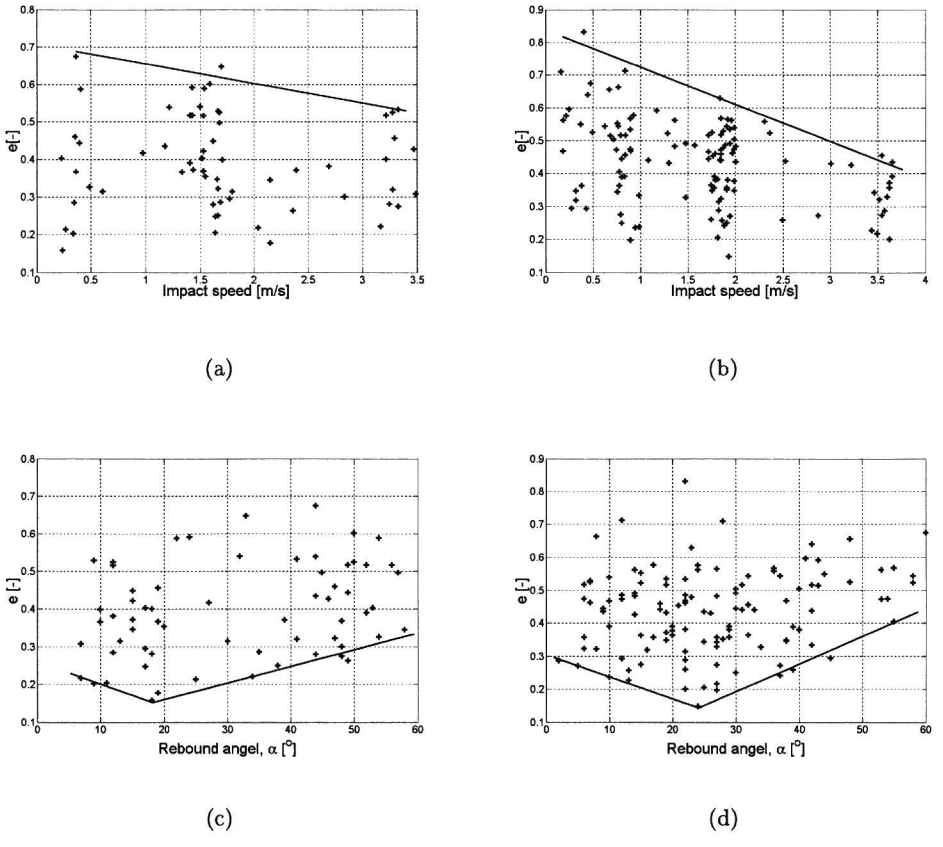

Figure 4.3: The coefficient of restitution versus impact speed, (a) 48h-sample, (b) N2-sample. The coefficient of restitution versus rebound angle, (c) 48h-sample, (b) N2-sample.

value of the coefficient of restitution for larger impact velocities. The decrease of e for larger impact velocities is also found by van Beek [1] and Abd-Elhady et al. [33]. A larger impact speed involves more plastic deformation and therefore more energy is lost [1]. The scattering in the coefficient of restitution is rather large. Figures 4.3c-d show the coefficient of restitution versus the rebound angle. Both graphs show a decrease in the minimum value of the coefficient of restitution until a rebound angle around 20°. After 20° an increase in the minimum value has been found.

4.1.3 Rebound angle

The coefficient of restitution depends on the rebound angle, as shown in the previous section. The value of the rebound angle depends on the place on the sphere where the impaction takes place. The rebound angle is measured for the incident particles that have fallen perpendicular on the sintered sample. Figure 4.4 shows a particle rebound in 3D.

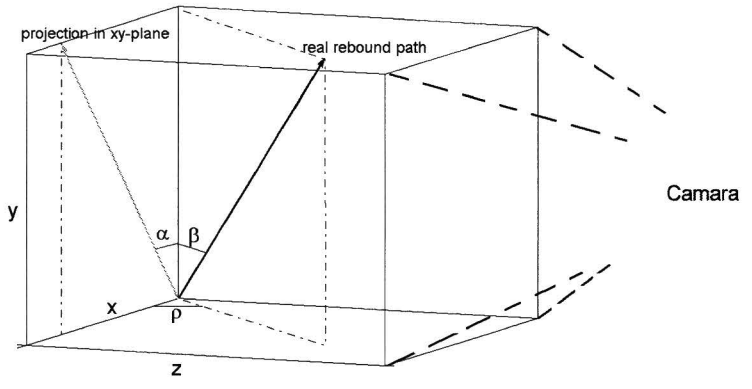

Figure 4.4: Schematic view of the real rebound angle β and observed rebound angle β.

The images taken with the camera are a projection of the real rebound path in the xy-plane. For a large number of images the rebound angle has been determined. Figure 4.5 shows the frequency distribution of the measured rebound angles for the 6h-sample, 48h-sample and N2-sample. The graphs show a peak around 20 degrees. A shift is noticeable for the 48h-sample from the angles between 55-60° to 50-55° in comparison with the 6h-sample. In order to understand the distributions found in figure 4.5 a model is derived.

Model

In the model slip, rotation, deformation or attraction of adhesion during an impact are not taken into account. The particles are positioned according to a cubic array. Every point on the surface of a sphere has a specific angle ϕ and ρ, see figure 4.6. On the sphere a grid is placed with grid distances $\Delta\phi$ and $\Delta\rho$. The real rebound angle depends only on ϕ. The real rebound angle β is,

$$\beta = 2\phi \tag{4.2}$$

Every section of the grid given by $\Delta\phi$ and $\Delta\rho$ represents a certain area on the sphere and a specific β. The ratio between the grid area and the total surface area gives the probability for the specific β. Calculate for every grid section the probability for β and a probability curve as function of the β can be made. The probability P is calculated as follow

$$P_{\phi_2-\phi 1} = \sin\phi_2{}^2 - \sin\phi_1{}^2 \tag{4.3}$$

With ϕ_1 and ϕ_2 the grid boundaries in ϕ-direction. Equation 4.3 shows that the probability increases for larger ϕ's and therefore also for larger larger β's. The experimental determine

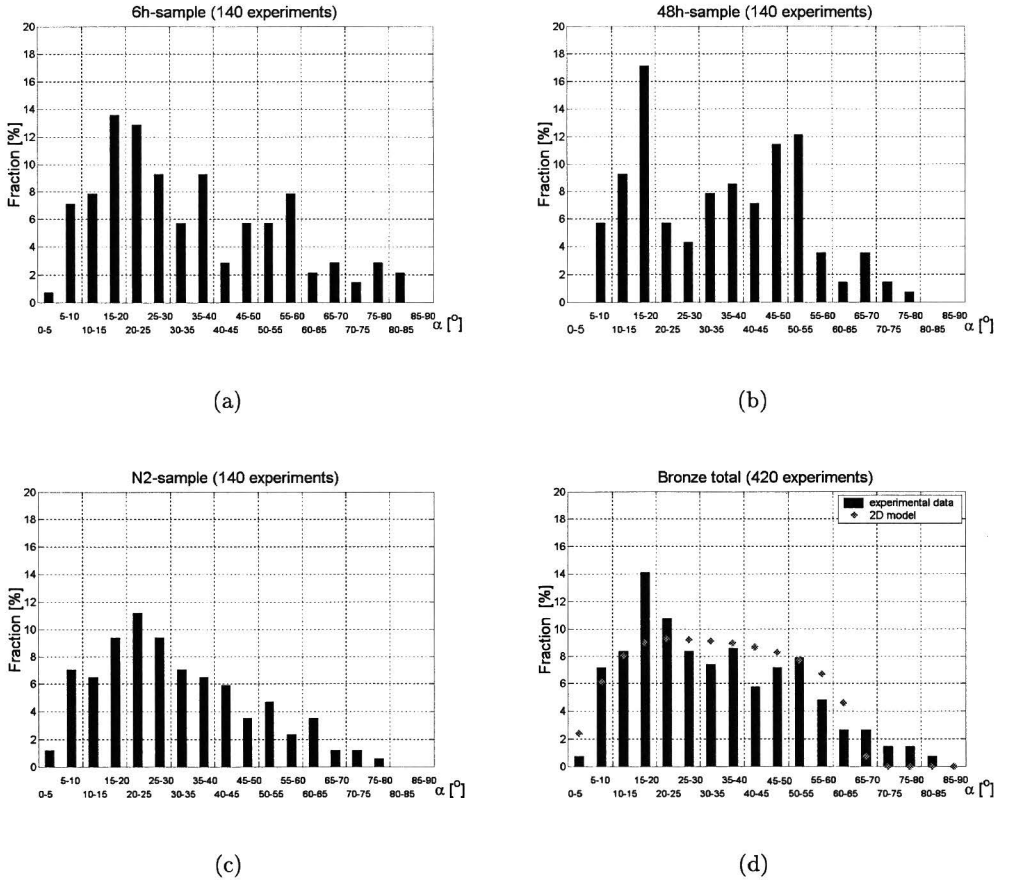

(a) (b)

(c) (d)

Figure 4.5: Distributions of the rebound angle

rebound angle shows only an increase until 20°, see figures 4.5.
The current capability of the experimental set-up is to follow a particle in 2D. So the real impact angle can not be observed as $\rho \neq 0$. The relation between α and β can be given as follow ;

$$\alpha = \arctan(\cos(\rho)\tan(\beta)) \tag{4.4}$$

When $\rho = 0$, $\alpha = \beta$ and $\rho = 90°$ $\alpha = 0$. A Matlab routine calculates for every grid section the corresponding α. Using equation 4.2 and 4.3 a probability curve as function of α can be made. Figure 4.5d shows for 420 experiments and for the model the frequency distribution. The predicted distribution agrees fairly well with the measured distribution. Only the large peak around 20° is not predicted.

The large amount of experimental data from figure 4.5d makes it possible to transform the observed rebound angles α back into a real rebound angles β. Each bar plotted in figure 4.5d contains n numbers of experiments. To calculate the real rebound angle equation 4.4 can be rewritten in,

$$\beta = \arctan\left(\frac{\tan(\alpha)}{\cos(\rho_i)}\right) \tag{4.5}$$

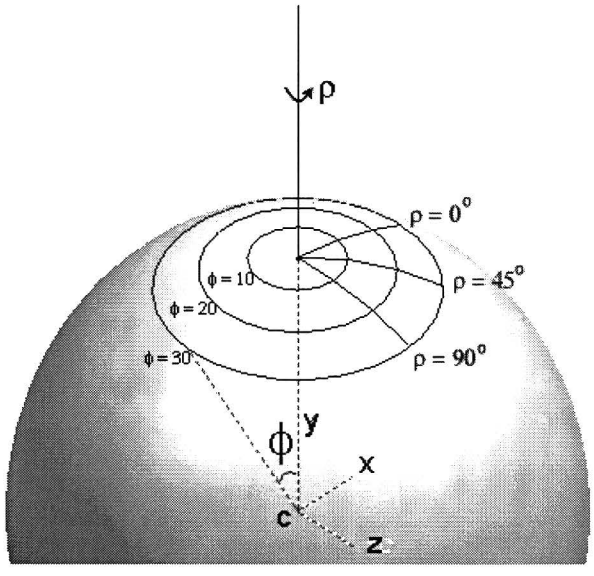

Figure 4.6: Schematical representation of the grid on the sphere surface.

With α measured and ρ_i varies between 0 - ρ_{max}. ρ_i depends on the numbers of experiments n. ρ_{max} is the angle where β becomes 60°. According to the assumption, particles with rebound angles larger than 60° hit in their rebound path a neighbor particle, this is not taken into account. From the calculated β's a frequency distribution is made, see figure 4.7. The model presented in this figure is made with equation 4.3. The transformed rebound angles show a plateau between 20 and 50°.

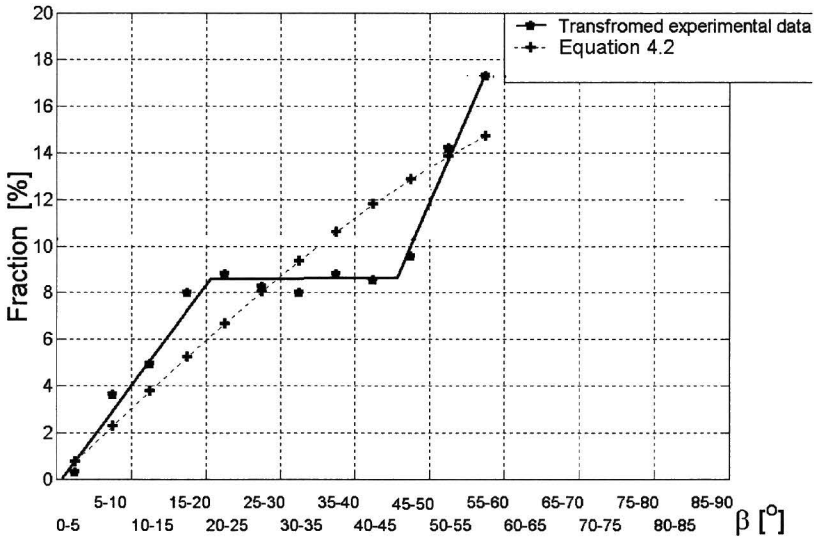

Figure 4.7: Distributions of the real rebound angle

4.2 Temperature gradient sintering experiments

To determine the influence of temperature gradient on the structure of a powder, an experiment is conducted that heats the top and cools the bottom of a powder. The results of these experiments are presented in table 4.2

Table 4.2: Temperature gradient experiments

Material	$\bar{T}_t$	$\bar{T}_b$	$\bar{T}_t - \bar{T}_b$	$\dot{m}$	s	P_t	P_b
	[°C]	[°C]	[°C]	[kg/s]	[mm]	[%]	[%]
Bronze 1h	209	82	127	0.04	4.4	40	40
Bronze 5h	213	111	102	0.04	7.2	35	39
Bronze 17h	213	77	136	0.01	8.8	32	40
Bronze 44h	185	72	113	0.05	6.1	30	38

Here is $\bar{T}_t$ the average top temperature of the sample, $\bar{T}_b$ the average bottom temperature of the sample, $\dot{m}$ the mass flow through the cooling channel, s the thickness of the sintered part, P_t the porosity of the top of the sintered part and P_b is the porosity of the bottom of the sintered part.
The following observations are made for all the experiments.

- The top temperature decreases in time, see figure 4.8b.
- The temperature difference between T_t and T_b decreases in time, see figure 4.8b.
- After the experiments, one part with thickness s is sintered, the other part is still powdery. The thickness of the sintered part increases with time, except for the 44h experiment.
- To control the temperature of the ceramic heater at 400 °C, fluctuations occur with an amplitude of ± 7 °C every 90 s. The frequency of the fluctuations keeps constant during the experiments. From this can be concluded that the power that is given of by the electric heater is constant every 90 s.
- The thermal conductivity increases in all the experiments, see figure 4.8a. For calculation of the relative thermal conductivity the average value is over a time period of 1h. The relative thermal conductivity is the ratio between the actual thermal conductivity of a porous structure and thermal conductivity of the solid material. Robinson et al. [36, 37] measured for ash deposits also an increase in the thermal conductivity when the temperature of the layer was above the minimum sintering temperature.
- Table 4.2 shows for the bronze experiments with longer sintering times an increase in top porosities. While the bottom porosity stays nearly constant. For sample 44h a gradual decrease of the porosity is found as a function of the sample height, see figure 4.9. Figures 4.10a-b show the difference in neck sizes between the bottom and the top of the 44h-sample.

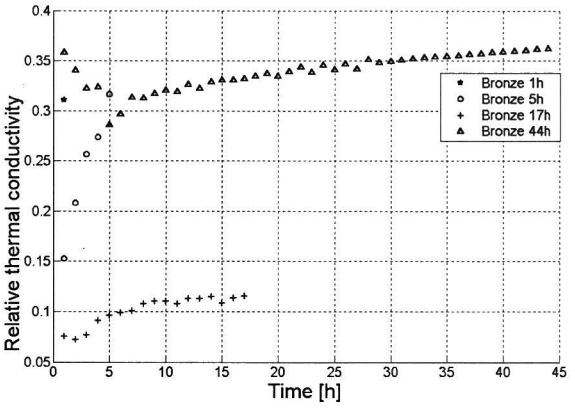

(a)

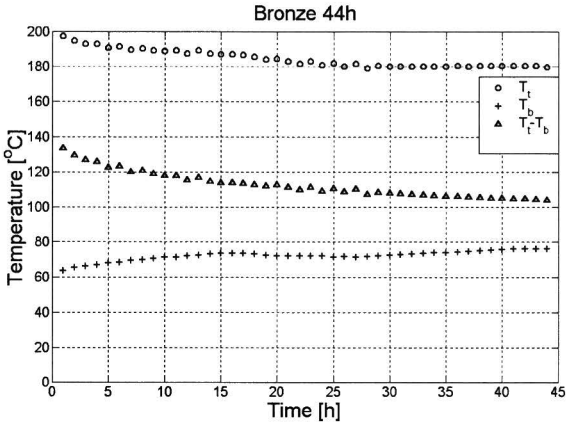

(b)

Figure 4.8: (a) The change of the relative thermal conductivity in time for the four bronze experiments. (b) Temperature measurements for bronze 44h experiment, the trend in the figure has also been found in the other experiments.

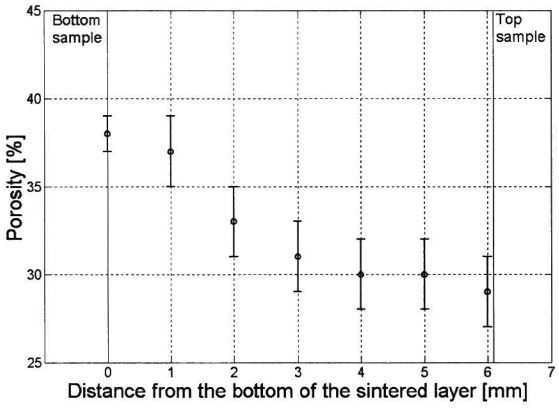

Figure 4.9: Porosity change in 44h-sample

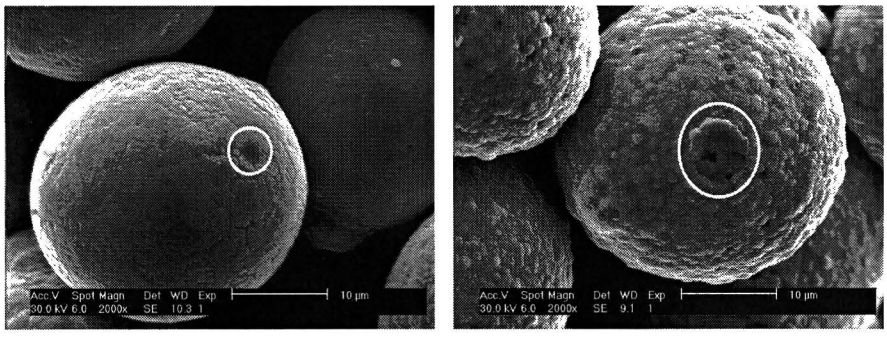

(a) (b)

Figure 4.10: Bronze 44h sample, the white circles mark the position of the neck. (a) SEM image bottom sample. (b) SEM image top sample.

4.3 Sintering in a gas cooler of a biomass gasifier

The influence of sintering is studied in a gas cooler of a biomass gasifier. The hot gasses coming from the biomass gasifier are cooled down from 950 °C to 450 °C through the gas cooler to produce steam for power production. The gas cooler consists of four consecutive sections, first evaporator, super heater, second evaporator and an economizer as shown in figure 4.11. From the biomass gasifier fly ashes ($> 1\ \mu m$) and aerosols ($< 1\ \mu m$) are emitted. These particles deposit on the gas cooler tubes. For the fouling layer of the first evaporator a porosity measurement is done. Also the minimum sintering temperature of the layer is determined. This temperature is compared with the gas-side temperature in the gas cooler.

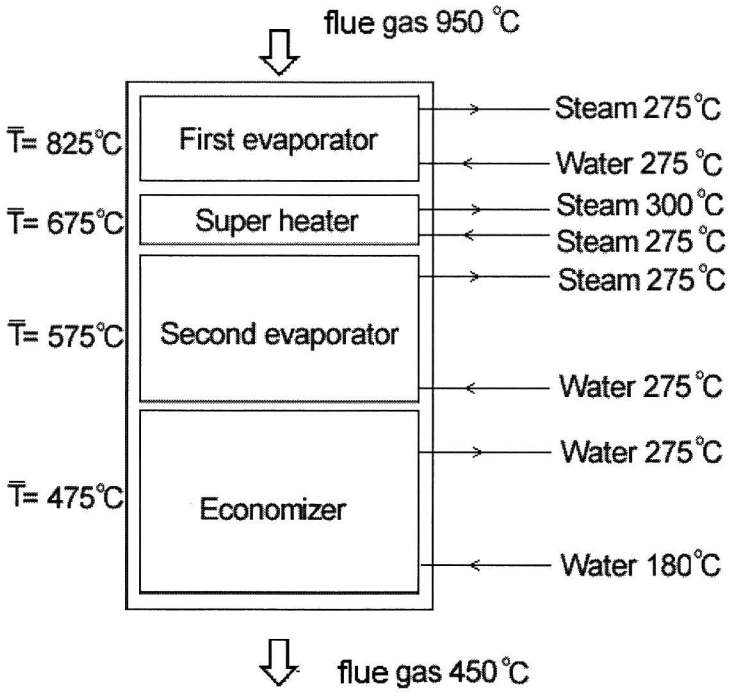

Figure 4.11: Different sections of the gas cooler. Temperatures on the left are the average gas-side temperatures of the specific sections. Temperatures on the right are the inlet and outlet temperatures of the water side of the specific sections.

Porosity measurement

A sample from the fouling layer from the first evaporator is imbedded in epoxy, cross sectioned and polished for SEM analysis. Figure 4.12 shows the result of the porosity measurement. Similar as for the temperature gradient experiment for the bronze particles a gradual decrease in porosity is measured as function of the height of the fouling layer. The difference in structure of the top and bottom of the layer is showed in figure 4.13. The top is condense and the bottom is powdery.

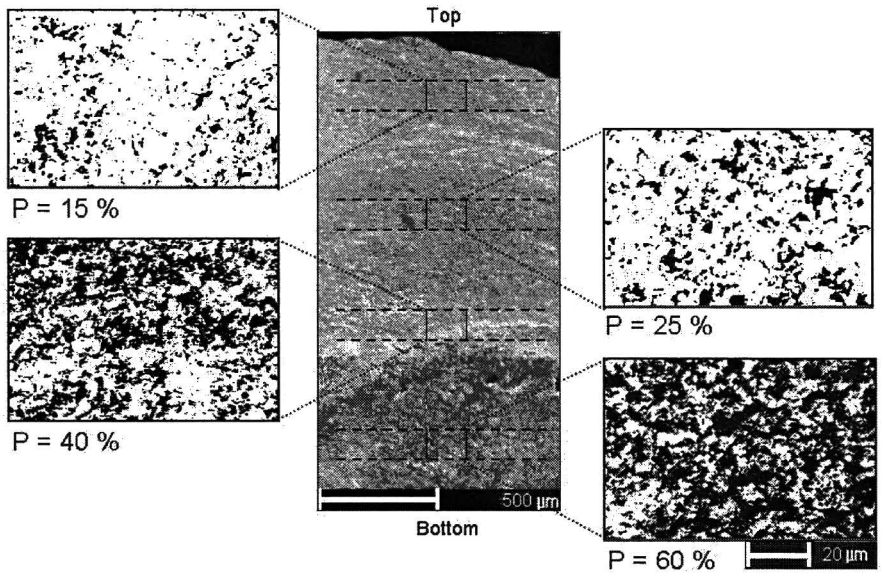

Figure 4.12: Porosity measurement at different sections of the fouling layer cross section. White represents material and black represents air (epoxy)

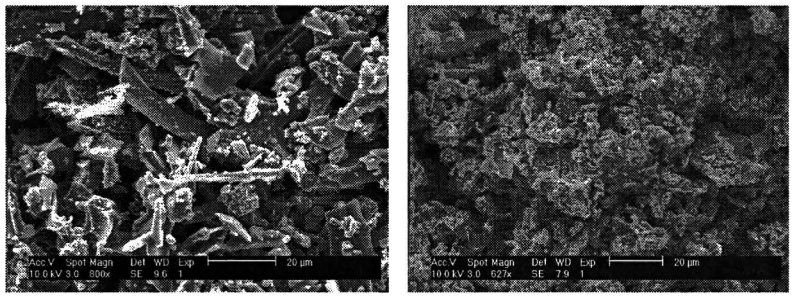

(a) (b)

Figure 4.13: (SEM images taken at different sections of the fouling layer. (a) Near the heat exchanger tube, i.e. bottom of the fouling layer. (b) Top of the fouling layer.

Minimum sintering temperature

Fouling layer material from the first evaporator and the superheater is used for determination of the minimum sintering temperature. The layers are crushed into powder with particles smaller than 56 μm. The powder is placed in a airtight alumina container, which prevent oxidation of elements such as carbon and evaporation of elements like lead and zinc.

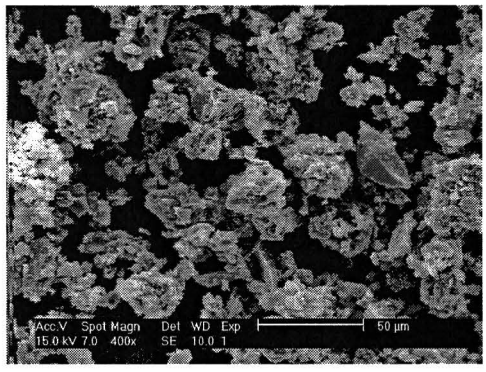

(a)

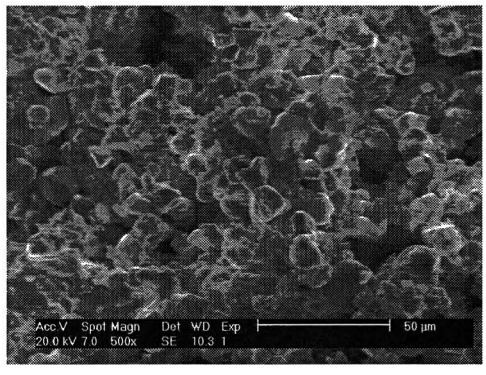

(b)

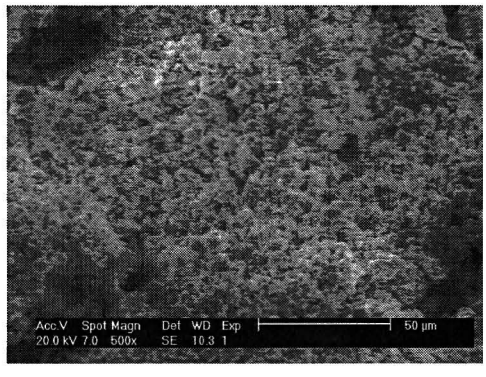

(c)

Figure 4.14: SEM images of the fouling layer particles heated for 20h at different temperatures. (a) Fouling layer at 650 °C, no sintering. (b) Fouling layer at 750 °C, sintering. (c) Fouling layer at 800 °C, sintering.

The experimental results of the minimum sintering temperature experiments are shown in figure 4.14. The fouling layer powder does not sinter at a temperature of 675 °C, see fig-

ure 4.14a. After this experiment the sample is still powdery and no particle agglomeration has been observed. Figure 4.14b shows that the heated particles has a condensed structure at a temperature of 750 °C. At a temperature of 800 °C a more condensed porous structure is found, see figure 4.14c. It can be concluded that the minimum sintering temperature for this fouling layer material is between 675 °C and 750 °C.
Only the average gas temperature of the first evaporator exceeds the minimum sintering temperature, see figure 4.11. Similar experiments are done for the fly ashes. The fly ashes are collected in a cyclone after the gas cooler. The fly ashes are heated up to temperatures as high as 1000 °C, but no sintering is observed. EDX (Energy Dispersive X-ray, surface element analysis) detects the presence of zinc and lead in the fouling layer, but not for the fly ashes. Zinc and lead seem to have a significant influence on the sintering process.

4.4 Discussion and conclusion

Impaction - sticking and removal

During an impact on a sintered layer less energy has been lost, due to less movement of particles compared to a powdery layer. Therefore the minimum velocity particles starts to rebound will decrease due to the sintering process. This behavior is observed in the impaction experiments, the minimum rebound velocity is for 1h-sample 0.16 m/s and for 48h-sample 0.08 m/s. The minimum sticking velocity for sintered bronze in N_2 is 0.04 m/s and for copper powder [33] with the same particle diameter is 0.17 m/s. Although the material properties of copper and bronze are slightly different, the difference in sticking behavior is rather significant.
More kinetic energy is necessary to remove particles out of the sintered surface in comparison to a powdery surface. A increase in the neck size means more energy is necessary to remove particles out of the surface. This is showed in figure 4.2.
Sintering decrease particle removal and can even stop removal for high degrees of sintering. Sintering influences the grow rate of the fouling layer by lowering the particle deposition rate and removal rate. The overlaps seen in figure 4.1 can be explained with impacts with different angles of impact and variation in neck area. The different behavior of the sintered bronze in air and in N_2 is caused by an oxidation layer. The oxidation layer will act as a energy absorber. This can be seen in the maximum sticking velocity, which are significant higher than the sticking velocity of the sintered sample in N_2. The large scattering for the coefficient of restitution is probably caused by the 2D-effect which influences the results of the coefficient of restitution and rebound angles.

Temperature gradient

A temperature gradient over a powdery layer causes different degrees of sintering as function of the layer thickness. A gradual decrease in the porosity from the top to the bottom is measured for sintered bronze and fouling layer sample. Sintering lowers the porosity

of the fouling layer and improves the contact between the particles, which is both beneficial for the thermal conductivity. Although the inaccuracy in the measurement of the thermal conductivity is rather large, all the experiments show a trend where the thermal conductivity increases with time.

Minimum sintering temperature

The minimum sintering temperature for the fouling layer material from the biomass gasifier is between 675-750 °C. EDX Element analysis detects the presence of zinc and lead in the fouling layer, but not for the fly ashes. Probably the aerosols that are emitted from the biomass gasifier contain a high amount of zinc and lead [38]. These aerosols deposit on the heat exchanger tubes. Due to the small size of the aerosols ($< 1\ \mu m$), the cyclone will not collect the aerosols and therefore no zinc and lead is found in the fly ashes.
The average gas-side temperature is 825 ° on the first evaporator, which ensures sintering to take place ensures sintering has taken place, see figure 4.11. For the other sections sintering will have no effect on the structure of the layer.

Chapter 5

Modelling of the breaking force for particle removal

From the impaction experiments can be concluded that particle removal depends on the impact speed of incident particle and the degree of sintering. In comparison with a powdery surface more kinetics energy is needed to remove particles out of a sintered surface. The force necessary to break the bonding between the particles depends on the degree of sintering. This breaking force, F_b, can be used for modelling particles removal from sintered surfaces. The two equations below describe the breaking force in normal and shear direction respectively,

$$F_{b_n} = \sigma_{max} A \tag{5.1}$$

$$F_{b_s} = \tau_{max} A \tag{5.2}$$

With σ_{max} and τ_{max} the maximum tensile and maximum shear stress respectively and A the breakage area. Equations 5.1 and 5.2 show that the breaking force depends on the breakage area. In section 5.1 the breaking area is determined using SEM-analysis. In section 5.2 the neck area is modelled for sintered glass and bronze particles using analytical sintering models. The chapter ends with discussions and conclusions in section 5.3

5.1 Fracture analysis

Fracture analysis have been done for sintered bronze particles in air and nitrogen and for sintered glass particles, see table 5.1. The samples are prepared as described in section 3.1.4. The sintered samples are manually broken and the fracture surface is analyzed under SEM.

An oxidation reaction has formed a oxidation layer on the surface of the bronze particles. The formed copper-oxide is very brittle compared to bronze [44]. The boundary between the bronze and the copper-oxide layer is the weakest part of the neck region, therefore the

Table 5.1: Sample properties

br_{air} sintered bronze in a hot air oven and br_{N_2} sintered bronze in nitrogen filled tube oven

Sintering time [h]	$X/D_{br_{air}}$ 200°C [−]	$X/D_{br_{air}}$ 400°C [−]	$X/D_{br_{N_2}}$ 500°C [−]	X/D_{gl} 600°C [−]
1	0.07	-	-	-
4	0.13	-	-	-
5	-	-	0.16	-
6	0.17	0.3	-	0.26
12	0.19	0.39	-	0.41
20	-	-	0.23	-
24	0.25	0.46	-	> 0.9
44	-	-	0.26	-
48	0.31	0.56	-	> 0.9

breakage happens at the boundary, as shown in the figures 5.1a-b. The Figures 5.1a-b show the most commonly observed fracture areas. Figure 5.1a shows a copper oxide fracture area and figure 5.1b show a bronze fracture area. The fracture area has the same size as the neck area.

To ensure no oxidation layer will form around the bronze particles, several samples are placed in a nitrogen tube oven, see table 5.1. Figure 5.1c shows two bronze particles sintered together. The fracture area, as shown in figure 5.1b, has again the same size as the neck area.

The breakage area for the sintered glass particles depends on the degree of sintering. Sintered glass particles for 6h show a similar behavior as the sintered bronze particles in nitrogen. For a sintered sample with a higher degree of sintering, like glass sintered for 12h, breakage will not necessarily take place along the necks, as shown in figure 5.1e.

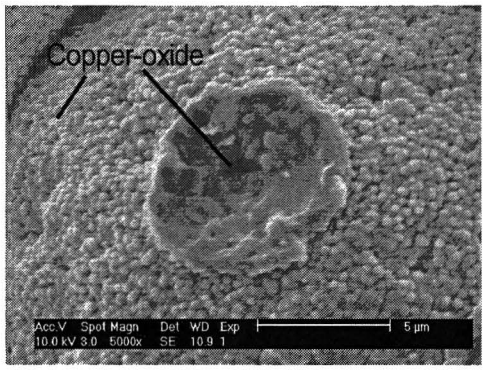

(a)

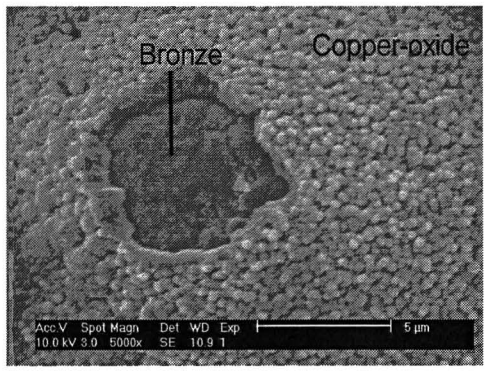

(b)

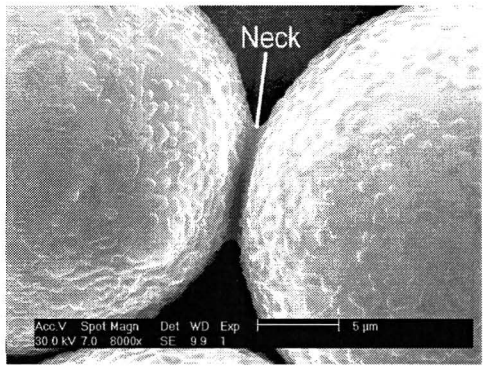

(c)

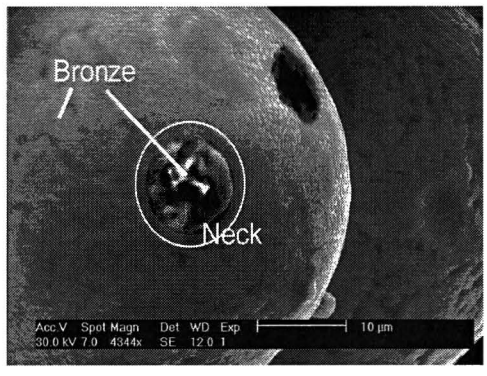

(d)

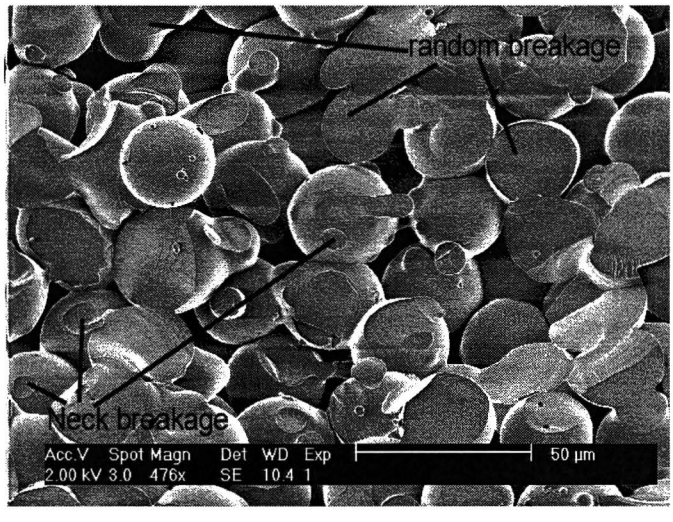

(e)

Figure 5.1: SEM image, (a) br_{air}, copper-oxide fracture area. (b) br_{air}, bronze fracture area (c) br_{N_2}, neck formation. (d) br_{N_2}, bronze fracture area. (e) Sintered glass 12h, random breakage

5.2 Modelling neck growth

It has been demonstrated in the previous section that the fracture area is equal to the neck area up to a certain X/D. The formed necks grow in time and grow faster with higher temperatures. The breaking force, necessary to break the bonding between the sintered particles, will therefore also increase with time. In order to determine the fracture area the neck area can be modelled. The fracture area can be used for determination of the breaking force, see equations 5.1 and 5.2. Finally the breaking force can be used in models that describe removal of particles from sintered layers, due to an incident particle impact. The analytical sintering models are used to model the neck growth of bronze and glass particles, see table 2.1. As described in section 2.3, a plot of $\log X/D$ versus $\log t$ shows a straight line. The slope of the line gives an indication, which sintering mechanism is dominant. In subsection 5.2.1 neck growth is modelled for sintered bronze particles. In subsection 5.2.2 neck growth is modelled for sintered glass particles.

5.2.1 Bronze

Figure 5.2 presents the neck growth of several bronze samples sintered at 200 and 400 °C for different times. The figure shows the influence of time and temperature influence on the neck growth. In figure 5.2 a straight line has been drawn through the experimental data. The slope of the line ($m = 3$) give reason to think that vapor transport is the dominant mechanism for the sintered bronze particles in air. 2.1.

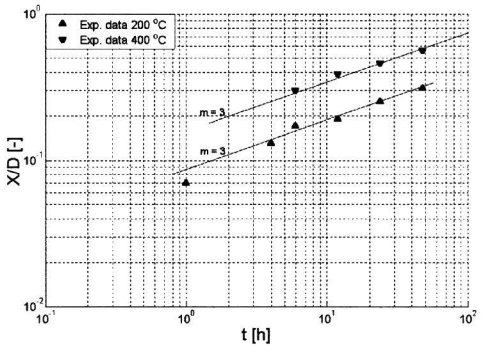

Figure 5.2: A straigth line through the experimental data shows, that the vapor transport is the dominant mechanism for sintered bronze in air.

For modelling neck growth with vapor transport the following model can be used [14].

$$\left(\frac{X}{D}\right)^3 = \left(\frac{3p_{vap}\gamma_{sv}}{\rho^2 D^2}\right)\left(\frac{\pi}{2}\right)^{\frac{1}{2}}\left(\frac{M}{R_c T}\right)^{\frac{3}{2}} t \tag{5.3}$$

With X the neck diameter, D the particle diameter, p_{vap} the vapor pressure, γ_{sv} the surface energy, ρ the density, M the molecular weight, R_c the universal gas constant and T the temperature. Equation 5.3 describes vapor transport in the initial stage [14]. Figure 5.3 shows for the experimental data and the results of the analytical model using equation

5.3. The vapor pressure in the equation is used for fitting the model with the experimental results (p_{vap} = 0.02 Pa for 200 ^oC and p_{vap} = 0.2 for 400 ^oC). The vapor pressure is rather high compared to the value found in literature, for copper and copper-oxide a vapor pressure of 0.0012 and 0.0018 Pa at temperature of 927 °C are found respectively [43]. The increase of the vapor pressure for higher temperatures was also found in literature [41].

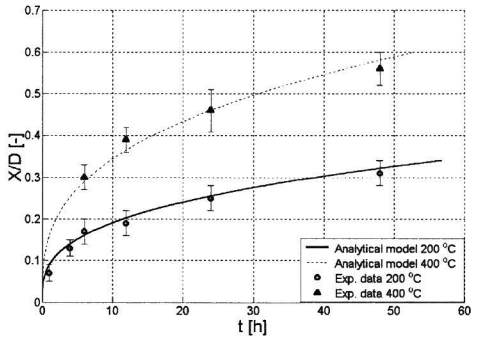

Figure 5.3: Bronze sintered in air is modelled with vapor transport.

In table 5.2.1 the experimental data are presented for sintered bronze in N_2. The large standard deviation makes it impossible to draw conclusions, which mechanism is dominant.

Table 5.2: Experimental data for sintered bronze in N_2 with a sintering temperature of 500 °C. Θ is the standard deviation for X/D

Sintering time [h]	X/D [-]	Θ [-]
5	0.16	0.07
20	0.23	0.05
40	0.26	0.07

5.2.2 Glass

Viscous flow describes the sintering behavior of glass particles [13]. In section 2.3 three analytical models are presented respectively for the initial stage, intermediate stage and final stage. Only Frenkels [13] initial stage model predicts neck growth. The other two viscous flow models calculate the density change with time.
For modelling neck growth of the sintered spherical glass particles Frenkels model has been used,

$$\left(\frac{X}{D}\right)^2 = \frac{3\gamma_{sv}}{\eta D}t \tag{5.4}$$

With η the viscosity. Figure 5.4 presents the experimental data for the glass particles heated at 600 °C for 6 and 12h. The solution of the analytical model is presented by the straight line and fit the experimental data with $\eta = 9\ 10^9$ Pa s. Similar experiments were done by Kuczynski, see figure 2.4.

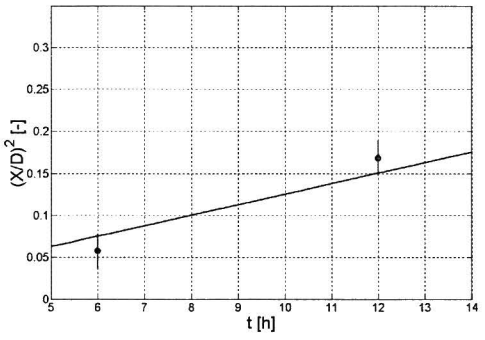

Figure 5.4: (a) Experimental data, glass sintered at 600 °C. The solution for the analytical model is presented with the straight line. A viscosity of $\eta = 9\ 10^9$ Pa s fits best the experimental data

Sintering experiments for have also been conducted for 24 and 48h. The high degree of sintering for these samples makes it impossible determine the neck size, see figure 5.5b. For glass particles sintered for 12h, the necks can still be recognized, see figure 5.5a.

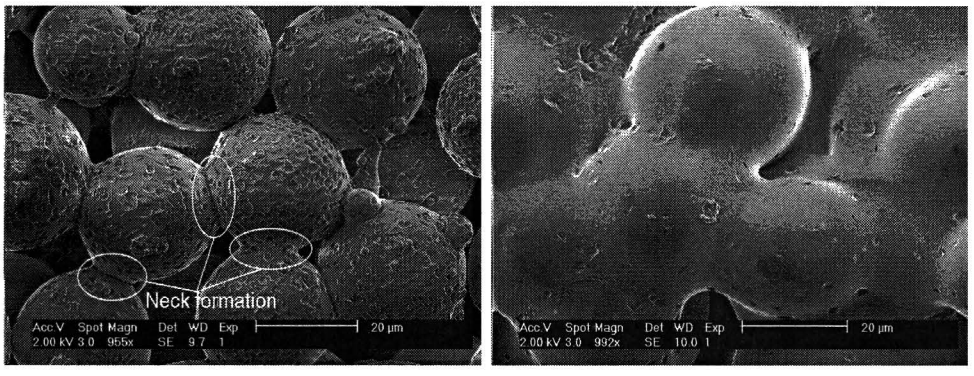

(a) (b)

Figure 5.5: Glass particles sintered at 600 °C. (a) 12h. (b) 24h.

5.3 Discussion and conclusions

It can be concluded from the two previous sections that neck area is equal to the breakage area up to a certain X/D. The neck area can be modelled for spherical particles using the analytical models from table 2.1, which are valid for X/D < 0.3. Particle removal from sintered surfaces can be predicted by following the scheme in figure 6.1. First the sintering rate has to be determined to see which mechanism is dominant. For spherical particle the method described in the section 2.3 can be used. For non-spherical particles the sintering rate can be determined using the measurement technique PDS as described in section 2.6. The dominant mechanisms can be modelled with the sintering models.

For sintering with non-spherical particles, atmospheric interaction, a wide particle size distribution or non linear heating, more sophisticated models have to be developed, see section 2.4. The breakage force can be implemented in models that describes removal of particles from fouling layers, due to an incident particle impact.

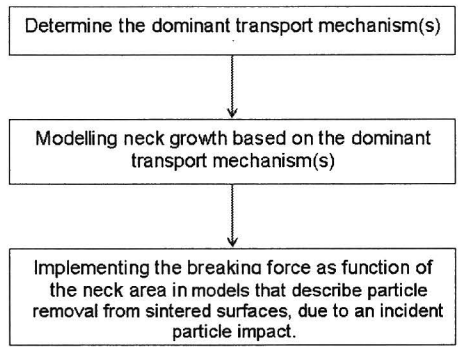

Figure 5.6: Schemetic overview for modelling particle removal from sintered surfaces

Chapter 6

Conclusions and recommendations

6.1 Conclusions

The structure of the fouling layer depends strongly on the gas-side temperature. Two types of fouling layers on the gas-side of the heat exchanger can be distinguished, namely powdery and sintered fouling layers. The fouling layer remains powdery if the gas-side temperature is below the minimum sintering temperature. The fouling layer will change into a robust porous structure, if the gas-side temperature exceeds the minimum sintering temperature. Particle deposition and removal by particle impaction differs significantly for sintered layers compared to powdery layers. Sintering causes neck formation to start at the contact point between particles. Due to the neck formation, the particles in the sintered layer can only move as a whole, which consequently reduces the energy losses, due to an incident particle impact and therefore lower the sticking velocity. Furthermore, particle bonding reduces the particle removal by particle impaction, because more kinetic energy is necessary to break the bonding between particles. Sintering influences the grow rate of the fouling layer by lowering the particle deposition rate and removal rate.
If the temperature of the flue gasses exceeds the minimum sintering temperature, the sintering process will change the microstructure on the top of the fouling layer. Sintering has relatively little effect on the bottom of the sintered fouling layer adjacent to the relatively cold heat exchanger tube. The temperature gradient over a fouling layer causes a gradual decrease in the porosity from the top (i.e. near the hot gas-side) to the bottom (i.e. near the cold waterside) of the layer. Sintering lowers the porosity and improves the contact between the particles, which are both beneficial for the thermal conductivity.
Sintering changes the microstructure of a fouling layer into a strong condense structure, this can be prevented if the gas-side temperature does not exceed the minimum sintering temperature of the fouling layer material.

6.2 Recommendations

Improvements on the experimental setups

Impaction experiments

For the impaction experiments the coefficient of restitution and rebound angle have been determined. Both parameters indicate, that a 2D-effect influences the results. To overcome this problem an additional camera has to be installed to follow the particles in 3D. The cameras have to be synchronized to be able to analyze the recorded images.

The current method for analyzing the recorded images is time consuming, therefore first attempts have been made for analyzing the recorded impaction images automatically. This must still be improved to be able to replace the time consuming manual analyzing method.

Temperature gradient experiment

The current cooling power of the temperature gradient setup create a homogenous temperature profile beneath the fouling layer sample. A homogenous temperature is preferred for establishing a well defined temperature gradient. The temperature rise of the cooling water in the cooling channel is too small to calculate an accurate thermal conductivity. A usable increase in the water temperature is expected if the volume of the cooling channel is reduced and the mass flow is lowered

Modelling of particles removal from sintered layers

The particles removal rate depends on the impact speed of the incident particles and the breaking force. The breaking force depends on the degree of sintering. This force can be modelled using sintering models that predicts neck growth. The neck growth can be modelled for spherical particles with analytical sintering models for $X/D < 0.3$. To be able to model sintering with a wide particle size distribution, non-linear heating, atmospheric interactions or liquid formations, more sophisticated numerical sintering models have to be developed. The breaking force can be implemented in models that describe particle removal from sintered surface, due to an incident particle impact, see figure 6.1.

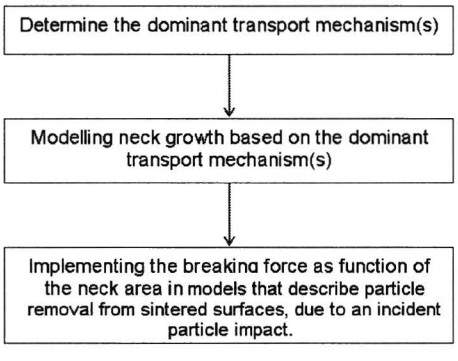

Figure 6.1: Schemetic overview for modelling particle removal from sintered surfaces

Bibliography

[1] M.C. van Beek. *Gas-Side Fouling in Heat-Recovery Boilers*,Phd, Technische Universiteit Eindhoven, Eindhoven, 2001.

[2] R.M. German. *Sintering theory and practice*, John Wiley & Sons Inc, New York, 1996.

[3] G.C Kuczynski. *Self-diffusion in Sintering of Metallic Particles*, Trans AIME, 1949, vol. 185, pp. 169.

[4] G.C. Kuczynski, D.P. Uskokovic, H Palmour III, M.M. Ristic. *Sintering '85*, Plenum Press, New York, 1985.

[5] M.M. Ristic. *Sintering - new developments*, Elsevier scientific publishing company, Amster- dam, 1979.

[6] M.N. Rahaman. *Ceramic processing and sintering*, Marcel Dekker Inc, New York, 1995.

[7] M.X. Barsoum. *Fundamentals of ceramics*, The Mccraw-Hill Companies, Inc, New York, 1997.

[8] D.W. Richerson. *Modern ceramic engineering*, 2nd ed., Marcel Dekker, New York, 1992.

[9] R.L. Coble. *Initial Sintering of Alumina and Hematite*, J. Am. Ceram. Soc., vol 41, pp 55, 1958.

[10] R.W. Cahn, P. Haasen, E.J. Kramer. *Materials Science and Technology, vol 17B, Processing of ceramics, part II*, VCH, Weinheim, 1996.

[11] Y.M. Chiang, D.P. Birnie, W.D. Kingery. *Physical Ceramics, Principles for Ceramics Science and Engineering*, John Wiley & Sons, Inc, New York, 1997.

[12] J. Reed. *Principles of ceramics processing*, 2nd ed., Wiley-Interscience, New York, 1995.

[13] Frenkel. *Viscous flow of crystalline bodies under the action of surface tension.* J. Phys. (Moscow) 9, 5, 1945, 385.

[14] W.D. Kingery and M. Berg. *Study of the Initial Stages of Sintering Solids by Viscous Flow, Evaporation-Condensation, and Self-diõusion*, J. Appl. Phys. vol. 26, pp 1205, 1955.

[15] C.J. Brinker, G.W. Scherer *SOL-GEL science*, Academic Press, Inc, New York, 1990.

[16] T. Kraft, h. Riedel *Numerical simulation of solid state sintering; model and application*, Journal of the European Ceramic Society, 24, 2004, 345-361.

[17] M. Braginsky, V. Tikare, E. Olevsky *Numerical simulation of solid state sintering* , International Journal of Solids and Structures, ARTICLE IN PRESS, 2004

[18] H. Zeming, L. Ma *Constitutive modeling of the densification and grain growth of fine-grained alumina ceramics* Materials Science and Engineering A, Volume 361, Issues 1-2, 25 November 2003, Pages 130-135

[19] K. Darcovich, L. Bera, K. Shinagawa *Particle size distribution effect in FEM model of sintering porous ceramics* , Materials Science and Engineering, A341, 2003, 247-255.

[20] K. Shinagawa *Micromechanical modelling of viscous sintering and a constitutive equation with sintering stress* Computational Materials Science, Volume 13, Issue 4, January 1999, Pages 276-285

[21] E. A. Olevsky. *Theory for sintering: from discrete to continuum*, Materials Science and Engi- neering, R23, 1998, p 41-100.

[22] R. A. Sutton and G. B. Schaffer *An atomistic simulation of solid state sintering using Monte Carlo methods* Materials Science and Engineering A, Volume 335, Issues 1-2, 25 September 2002, Pages 253-259

[23] G.A.L. van de Vorst *Modelling and numerical simulation of viscous sintering* Phd thesis, Technische Universiteit Eindhoven, 1994.

[24] P. Compo, R. Pfeffer, G.I. Tardos, *Minimum Sintering Temperature and Defluidization characteristic of fluidizable particles*, Powder Technology, vol. 51, pp. 85-101, 1987.

[25] B.J. Skrifvars, M. Hupa, A. Moilanen, R lundqvist, *Characterization of biomass ashes*, Proc. of the Engineering Foundation Conference: The application of advanced technology to ash related problems in boilers, Waterville Valley, NH, USA, 1995.

[26] B.-J. Skrifvars and M. Hupa, *Sintering of Ash During Fluidized Bed Combustion*, Ind. Eng. Chem. Res., vol. 31, pp. 1026-1030, 1992.

[27] B.-J. Skrifvars and M. Hupa, *The Effect of Reducing Conditions on Coal Ash Sintering*

[28] P. Basu. *A Study of Agglomeration of Coal-Ash in Fluidized Beds*, Can. J. Chem Eng, vol 60, pp 791, 1982.

[29] A.Y. Al-Otoom, G.W. Bryant, L.K. Elliott, B.J. Skrifvars, M. Hupa, T. F. Wall, *Experimental Options for Determining the Temperature for the Onset of Sintering of Coal Ash*, Energy & Fuels 2000, 14, 227-233.

[30] Ervin E. Underwood, *Quantitative stereology*, Addison-Wesley Publishing Company, Massachusetts, 1970.

[31] E. A. Olevsky, G. A. Shoales, R. M. German. *Temperature effect on strength evolution under sintering*, Materials Research Bulletin 36, 2001, 449-459.

[32] A. Y. Al-Otoom, L. K. Elliott, T. F. Wall, and B. Moghtaderi *Measurement of the Sintering Kinetics of Coal Ash* ,Energy & Fuels, 2000, 14(1), 227-233

[33] M. S. Abd-Elhady, C. C. M. Rindt, J. G. Wijers and A. A. van Steenhoven *Particulate fouling in waste incinerators as influenced by the critical sticking velocity and layer porosity*, Energy, In Press, May 2004,

[34] M. S. Abd-Elhady, C. C. M. Rindt, J. G. Wijers and A. A. van Steenhoven *Removal of Particles from a Powdery Fouled Surface due to Impaction*, http://services.bepress.com/eci/heatexchanger/18/ - Santa Fe, New Mexico, USA, May 18-22, 2003

[35] M.S. Abd-Elhady, C.C.M. Rindt, J.G. Wijers, A.A. van Steenhoven, E.A. Bramer, Th.H. van der Meer *Inlfuence of heat exchangers operating gas temperature on particulate fouling*, International Journal of Heat and Mass Transfer, Volume 47, Issues 17-18, August 2004, Pages 3943-3955

[36] A.L. Robinson, S.G. Buckley, L.L. Baxter, *Minimum gas speed in heat exchangers to avoid particulate fouling* , Energy & Fuels, 2001, 15, 66-74.

[37] A.L. Robinson, S.G. Buckley, N. Yang, L.L. Baxter, *Experimental Measurements of the Thermal Conductivty of Ash Deposits: Part 2. Effect of Sintering and Deposit Microstructure*, Energy & Fuels, 2001, 15, 66-74.

[38] I.Obernberger. *Aerosols in fixed-bed biomass combustion -formation, growth, chemical composition, deposition, precipitation and separation from flue gas*, Proceedings, 2003.

[39] M.S. Abd-Elhady, S.H. Clevers, T.N.G. Adriaans, C.C.M. Rindt, J.G. Wijers, A.A. van Steenhoven, *Influence of operating gas-side temperature on particulate fouling of heat exchangers* sent to FUEL, Aug 2004.

[40] A.H. Kharaz, D.A. Gorham, A.D. Salman *An experimental study of the elastic rebound of spheres*, Powder Technology, Volume 120, Issue 3, 22 October 2001, Pages 281-291

[41] J. Paasivirta, S. Sinkkonen, P. Mikkelson, T. Rantio and F. Wania, *Estimation of vapor pressures, solubilities and Henry's law constants of selected persistent organic*

pollutants as functions of temperature, Chemosphere, Volume 39, Issue 5, August 1999, Pages 811-832.

[42] S.C. Kweon, E. Ramer, A.L. Robinson *Measurement and Simulation of Ash Deposit Microstructure*, Energy & Fuels 2003, 17, 1311-1323.

[43] C. Ludwig, A. J. Schuler, J. Wochele, S. Stucki *Measuring Heavy Metals by Quantitative Thermal Vaporization*, PAUL SCHERRER INSTITUT, http://people.web.psi.ch/ludwig/eco99.pdf, 2004

[44] S.H. Lahiri, N.K. Waalib Singh, K.W. Heng, L. Ang, L.C. Goh. *Kinetics of oxidation of copper alloy leadframes*, Micoelectronics Journal, 29, 1998, 335-341.

Appendix A

Particle size distribution

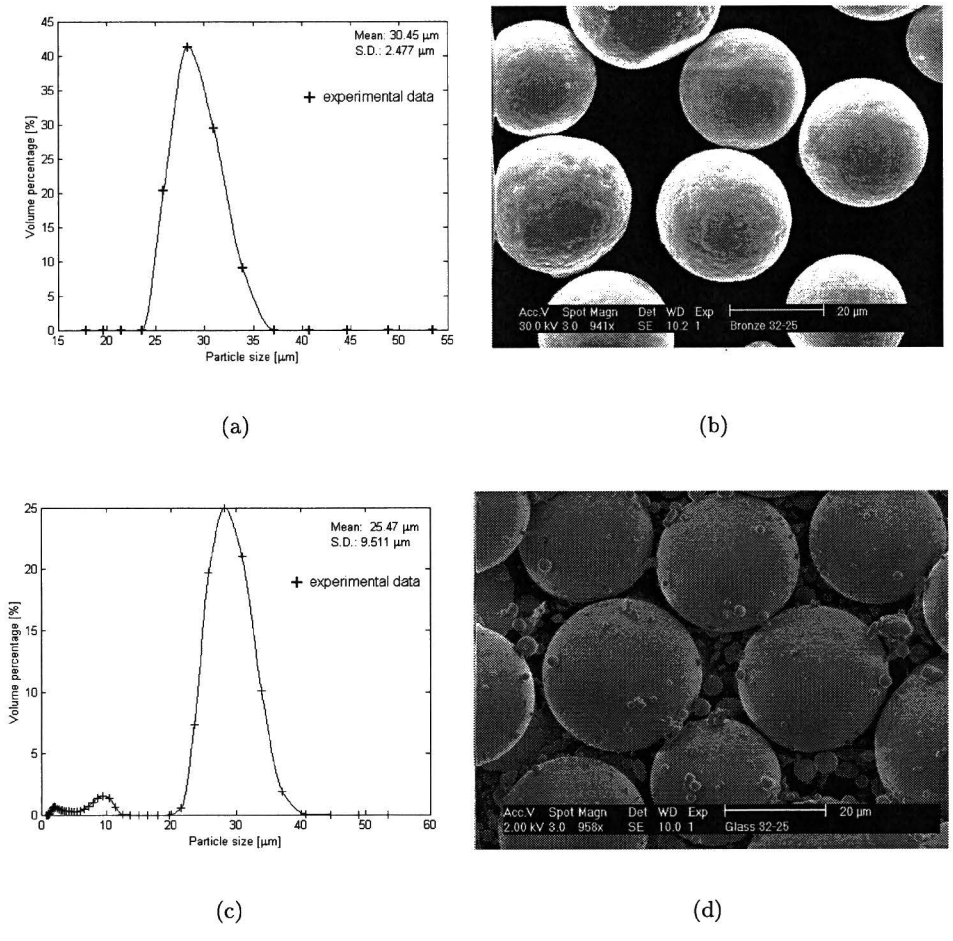

(a) (b)

(c) (d)

Figure A.1: (a) Particle distribution of the bronze particles. (b) Bronze particles. (c) Particle distribution of the glass particles. (d) Glass particles.

Appendix B

Temperature gradient setup

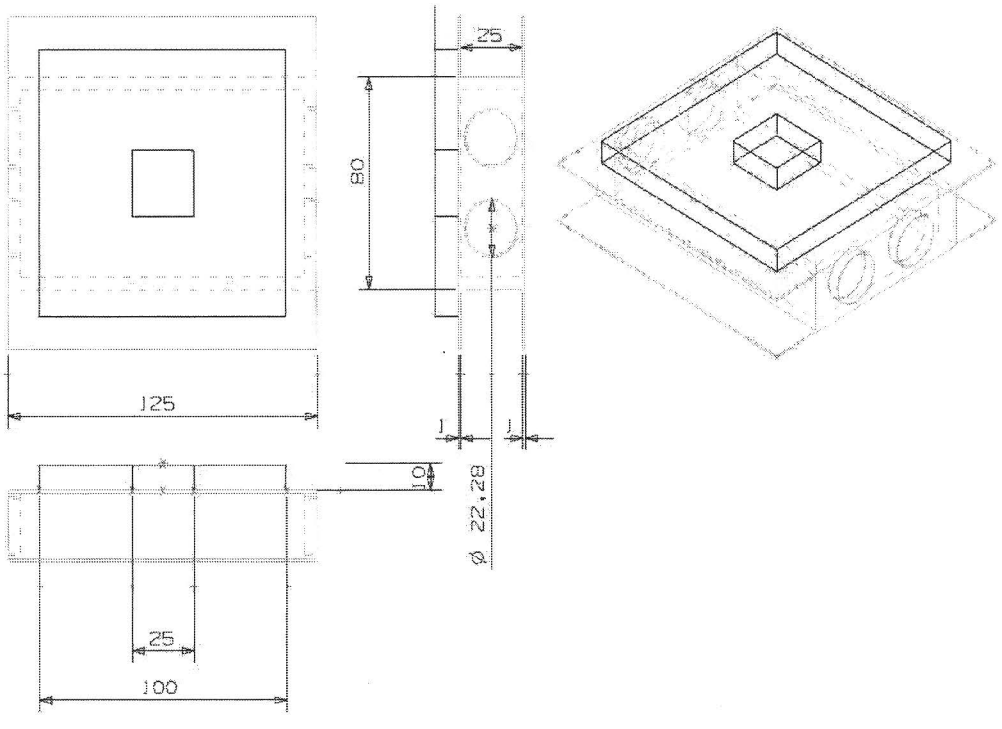

Figure B.1: Dimension are mm. The cooling channel and the sample holder.

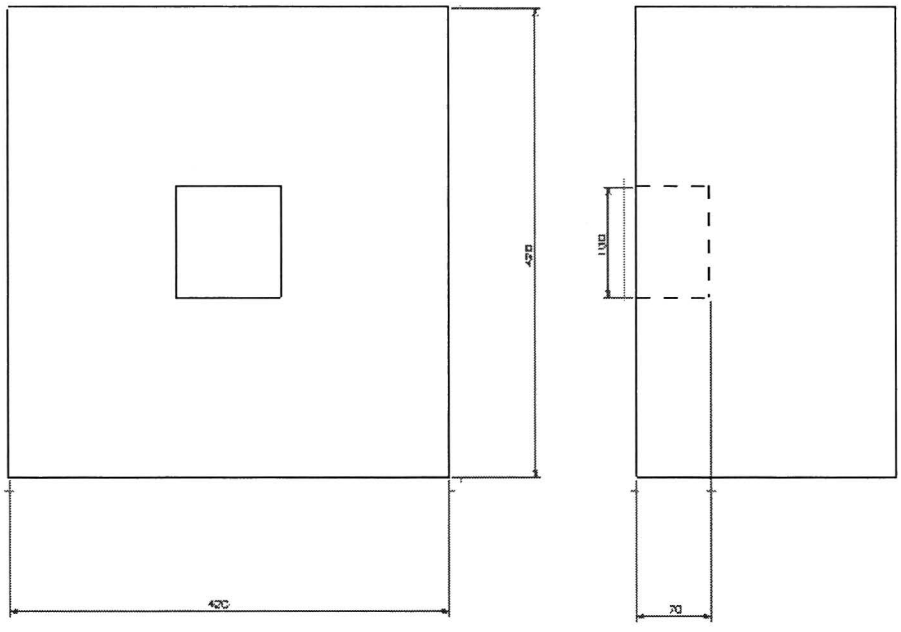

Figure B.2: Dimension are mm. The oven

Appendix C

Experimental results impaction experiments

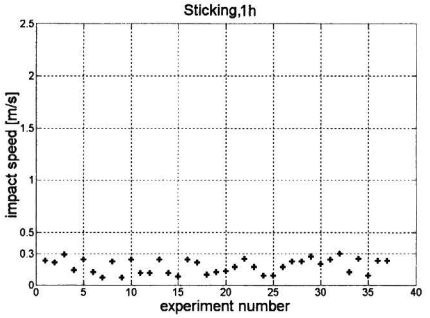
Sticking,1h
impact speed [m/s]
experiment number

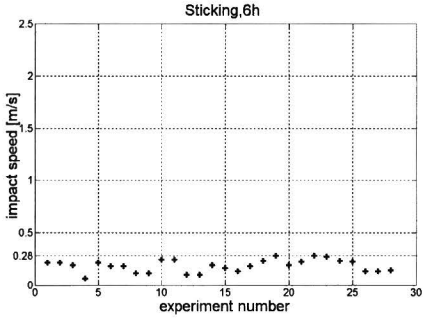
Sticking,6h
impact speed [m/s]
experiment number

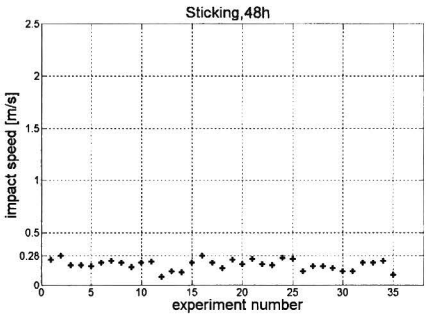
Sticking,48h
impact speed [m/s]
experiment number

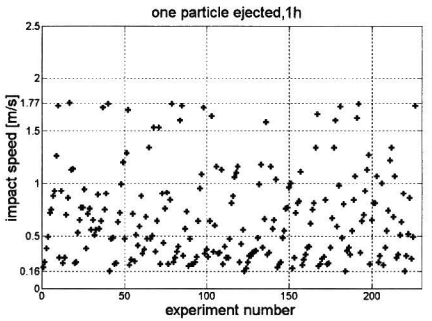
one particle ejected,1h
impact speed [m/s]
experiment number

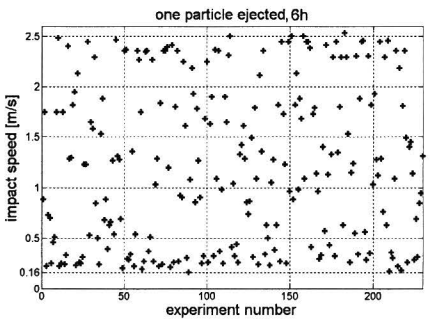
one particle ejected,6h
impact speed [m/s]
experiment number

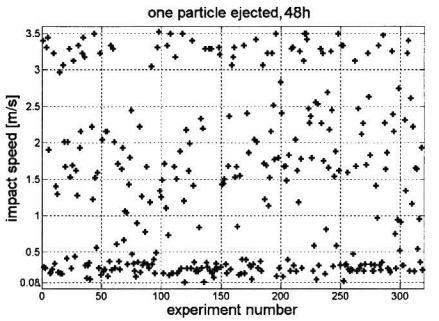
one particle ejected,48h
impact speed [m/s]
experiment number

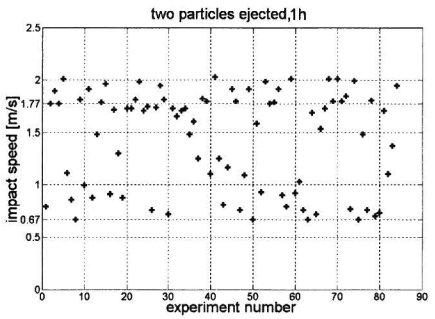
two particles ejected,1h
impact speed [m/s]
experiment number

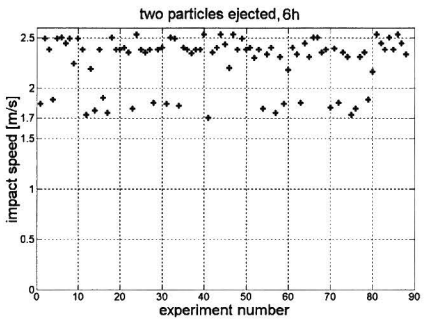
two particles ejected,6h
impact speed [m/s]
experiment number

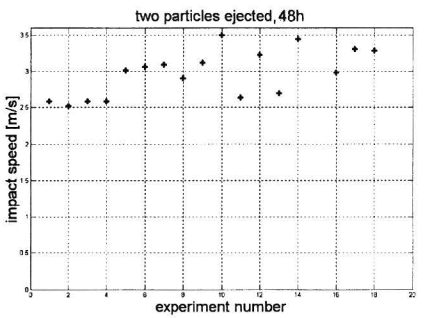
two particles ejected,48h
impact speed [m/s]
experiment number